Non-Hermitian Numerical Renormalization Group: Solution of the Non-Hermitian Kondo Model

Phillip C. Burke and Andrew K. Mitchell

School of Physics, University College Dublin, Belfield, Dublin 4, Ireland
and Centre for Quantum Engineering, Science, and Technology, University College Dublin, Dublin 4, Ireland

(Received 16 April 2025; revised 17 June 2025; accepted 17 October 2025; published 12 November 2025)

Non-Hermitian (NH) Hamiltonians describe open quantum systems, nonequilibrium dynamics, and dissipative processes. Although a rich range of single-particle NH physics has been uncovered, many-body phenomena in strongly correlated NH systems have been far less well studied. The Kondo effect, an important paradigm for strong correlation physics, has recently been considered in the NH setting. Here, we develop an NH generalization of the numerical renormalization group and use it to solve the NH Kondo model. Our nonperturbative solution applies beyond weak coupling, and we uncover a nontrivial phase diagram. The method is showcased by application to the NH pseudogap Kondo model, which we show supports a completely novel phase with a genuine NH stable fixed point and complex eigenspectrum. Our NH numerical renormalization group code, which can be used in regimes and for models inaccessible to, e.g., perturbative scaling and Bethe ansatz, is provided open source.

DOI: 10.1103/19td-1k9s

The past two decades have seen immense interest in open quantum systems, with non-Hermitian (NH) Hamiltonians describing the effective dynamics of dissipative systems playing a key role [1–5]. NH Hamiltonians present certain unique challenges, such as dealing with complex eigenvalues, nonorthonormal eigenvectors [6,7], and exceptional points [8–18]—singularities in parameter space at which eigenvalues and eigenstates coalesce. NH systems with $\mathcal{PT}$ symmetry [19–21] are somewhat simpler, having real eigenvalues, but many systems of interest do not fall into this class. Much attention has, to date, focused on single-particle NH systems [3,4], while many-body counterparts remain far less well explored. Although recent work has begun to address strongly correlated NH physics, nonperturbative numerical methods beyond exact diagonalization remain limited [22,23].

The Kondo model [24] is a classic paradigm for strong-correlation physics in the standard Hermitian scenario, so the solution of its NH generalizations is naturally of importance for understanding NH physics in the many-body context. Furthermore, as shown in Ref. [25], ultracold atom systems undergoing inelastic scattering with two-body losses can be described by an effective NH Kondo model. These factors have stimulated considerable interest in a range of NH quantum impurity models [25–41].

The non-Hermitian Kondo model reads

$$\hat{H} = \hat{H}_{\text{bath}} + J\hat{\boldsymbol{S}}_i \cdot \hat{\boldsymbol{S}}_0, \tag{1}$$

where $J = J_R - iJ_I$ is taken to be complex, $\hat{\boldsymbol{S}}_i$ is a spin-$\frac{1}{2}$ operator for the impurity, $\hat{H}_{\text{bath}} = \sum_{k,\sigma} \epsilon_k c^\dagger_{k\sigma} c_{k\sigma}$ describes a continuum bath of noninteracting conduction electrons labeled by spin $\sigma = \uparrow, \downarrow$ and momentum k, and $\hat{\boldsymbol{S}}_0 = \frac{1}{2}\sum_{\sigma,\sigma'} c^\dagger_{0\sigma} \boldsymbol{\tau}_{\sigma,\sigma'} c_{0\sigma'}$ is the local conduction electron spin density at the impurity position (here, $c_{0\sigma} = \sum_k \alpha_k c_{k\sigma}$ and $\boldsymbol{\tau}$ is the Pauli vector). The bath is characterized by its density of states at the impurity, $\rho(\omega)$. For a standard metallic flat band, we take $\rho(\omega) = \rho_0 \Theta(D - |\omega|)$. Equation (1) does not possess $\mathcal{PT}$ symmetry and so generically has a complex eigenspectrum.

The standard Hermitian Kondo model is recovered for $J_I = 0$. For antiferromagnetic coupling $J_R > 0$, the impurity spin is dynamically screened by surrounding conduction electrons via the Kondo effect [24] at low temperatures $T \ll T_K$, with $T_K \sim De^{-1/\rho_0 J_R}$ the Kondo temperature. The physics is nonperturbative and non-Markovian: even for small bare J_R, the impurity becomes strongly coupled to the bath at low T by formation of a many-body Kondo singlet state inside a large entanglement "cloud" [42–44]. The Kondo effect can be understood in the renormalization group (RG) framework [45] as a flow from the unstable local moment (LM) fixed point, corresponding to a free spin on the impurity decoupled from the bath, to the stable strong-coupling (SC) fixed point in which the impurity is bound up in the Kondo singlet. A full, nonperturbative solution of the Kondo problem is provided by Wilson's numerical renormalization group (NRG) technique [46,47], which can also be applied to generalized quantum impurity problems, and works with arbitrary bath density of states. The Hermitian Kondo model in the wide flat-band limit can also be solved exactly by Bethe ansatz [48].

The NH Kondo model was studied in Ref. [25] using a combination of perturbative scaling and Bethe ansatz, which provides a rather complete picture of the weak-coupling physics up to $|J|/D \lesssim 0.25$, beyond which the methods break down. It was shown that sufficiently strong dissipation (tuned by increasing J_I) can produce a quantum phase transition between the standard Kondo SC phase and an unscreened LM phase, via a mechanism analogous to the continuous quantum Zeno effect [49]. A reversion of the RG flow was observed in the LM phase, which violates the g theorem for Hermitian systems [50]. The low-energy fixed points were found to be real, meaning that the metallic NH Kondo model has an emergent Hermiticity. However, this scenario has recently been challenged, with the alternative Bethe ansatz results of Ref. [28] appearing to show a different phase diagram, with a new phase intervening between SC and LM.

In this Letter, we introduce the non-Hermitian numerical renormalization group (NH-NRG) method, which is fully nonperturbative, and can be applied to a wide range of Kondo or Anderson-type impurity models and their variants. With no restriction on coupling strength, we uncover a nontrivial phase diagram for the NH Kondo model [Fig. 1(a)], showing that at weak-to-moderate coupling, the scenario of Ref. [25] pertains. However, for stronger dissipation (larger values of J_I) we find reentrant Kondo behavior, whereas the LM phase is found to terminate entirely beyond a critical value of J_R. Unlike the Bethe ansatz and other methods such as conformal field theory that rely on linear dispersion [48,50], NH-NRG works with equal ease for any bath density of states. We apply NH-NRG to an NH pseudogap Kondo model, showing that the lower-critical dimension of the Hermitian model [51] is shifted by finite J_I, and an entirely new stable fixed point appears that is fundamentally non-Hermitian.

Non-Hermitian NRG—Here, we generalize the standard NRG methodology to treat NH quantum impurity problems. Although the basic algorithm proceeds along similar lines to Wilson's original formulation for Hermitian systems [46,47], incorporating NH physics involves additional challenges. Below we describe the key points, but full technical details and validation checks are given in the End Matter and Supplemental Material [52].

In the standard NRG procedure for the Kondo model, the first step is to logarithmically discretize the free conduction electron bath and map it to a 1D Wilson chain (WC). This is done by dividing up the density of states $\rho(\omega)$ into intervals according to the discretization points $\pm D\Lambda^{-n}$, where $\Lambda > 1$ is the NRG discretization parameter and $n = 0, 1, 2, 3, \ldots$. The continuous electronic density in each interval is replaced by a single pole at the average position with the same total weight, yielding $\rho_{\text{disc}}(\omega)$. We then map $\hat{H}_{\text{bath}} \to \hat{H}_{\text{WC}} = \sum_{n=0}^{\infty} \sum_{\sigma} (\epsilon_n f_{n\sigma}^{\dagger} f_{n\sigma} + t_n f_{n\sigma}^{\dagger} f_{n+1\sigma} + t_n f_{n+1\sigma}^{\dagger} f_{n\sigma})$ with the real parameters $\{\epsilon_n\}$ and $\{t_n\}$ chosen such that the local density of states at orbital $f_{0\sigma}$ to which the impurity couples is precisely $\rho_{\text{disc}}(\omega)$. Because of the logarithmic discretization [46], the WC parameters decay asymptotically as $\sim D\Lambda^{-n/2}$. We now define a sequence of Hamiltonians $\hat{H}_N$ comprising the impurity and the first N chain sites, satisfying the recursion relation $\hat{H}_N = \hat{H}_{N-1} + \hat{T}_N$, where $\hat{T}_N = \sum_{\sigma} (\epsilon_N f_{N\sigma}^{\dagger} f_{N\sigma} + t_{N-1} f_{N-1\sigma}^{\dagger} f_{N\sigma} + t_{N-1} f_{N\sigma}^{\dagger} f_{N-1\sigma})$. The

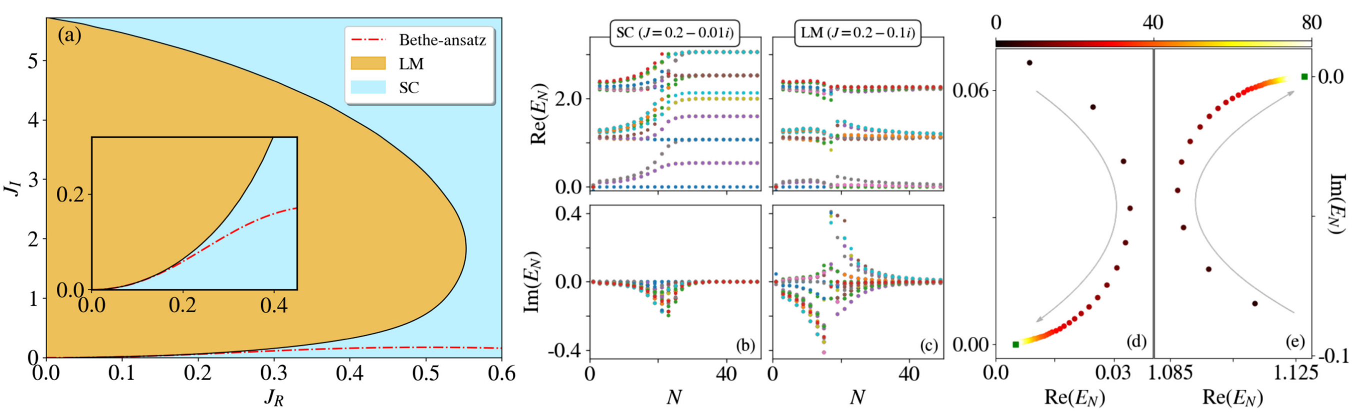

FIG. 1. Solution of the non-Hermitian Kondo model using NH-NRG. (a) Phase diagram in the (J_R, J_I) plane, showing the numerically exact boundary (black line) separating SC (blue) and LM (orange) phases. Red dot-dashed line shows the Bethe ansatz result [25], which is valid for $|J| \lesssim 0.25$ and agrees perfectly with NH-NRG in that regime (see inset). (b),(c) RG flow of the NH-NRG complex eigenvalues E_N with iteration number N, showing the real and imaginary parts in the top and bottom panels, for representative systems in the SC and LM phases. (d),(e) Illustration of the reversion of the eigenvalue RG flow in the Argand plane for two representative eigenvalues of the system in the LM phase ($J = 0.1 - 0.5i$). The iteration N (colorbar) increases in the direction of the arrows toward the Hermitian Kondo fixed point value (green point). Shown for different representative states in (d) and (e). NH-NRG calculations performed for $\Lambda = 3$ and $N_k = 400$.

sequence is initialized by $\hat{H}_0 = J\hat{\boldsymbol{S}}_i \cdot \hat{\boldsymbol{S}}_0$ [53] and the full (discretized) model is obtained as $N \to \infty$. Starting from the impurity, we build up the chain by successively adding WC sites using this recursion. At each step N, the Hamiltonian $\hat{H}_N$ is diagonalized, and only the N_k lowest energy states are retained to construct the Hamiltonian $\hat{H}_{N+1}$ at the next step. In such a way, we focus on progressively lower energy scales with each iteration. The higher energy states can be discarded at each step due to the energy-scale separation down the chain. The RG character of the problem can be seen directly in the evolution with N of the many-particle NRG energy levels of $\hat{H}_N$. This is done by specifying the NRG energies E_N with respect to the ground state energy of that iteration, and then rescaling by a factor $\Lambda^{N/2}$, so that the N_k retained states at each step always span the same energy range. Importantly, the NRG energy levels flow between fixed points (e.g., from LM to SC). The calculation scales linearly in N, and the stable fixed point is reached after a finite number of steps. NRG is thus able to capture an exponentially wide range of energy scales, from the bandwidth D down to the Kondo temperature T_K.

In the NH case, $\hat{H}_N$ in general has complex eigenvalues, and its left and right eigenvectors are distinct. The iterative diagonalization procedure in NH-NRG proceeds similarly to the Hermitian case, but the recursion by which $\hat{H}_{N+1}$ is obtained from $\hat{H}_N$ must be carefully reformulated to account for these crucial differences—see End Matter and [52]. One may construct a biorthonormal basis [6] if the spectrum is nondegenerate, and this provides substantial advantages in terms of the efficiency and stability of the algorithm. Although quantum impurity models do typically have many eigenvalue degeneracies, the most significant source of these is from symmetries. However, these symmetries can then be utilized to block-diagonalize the Hamiltonian in distinct quantum number subspaces [54]. In the present setting, labeling states by the total charge Q and total spin projection S_z is sufficient to separate all exact degeneracies into different blocks [56]. It is anyway desirable to exploit symmetries in this way since it reduces block sizes, and increases computational efficiency [57]. We identify two other sources of approximate degeneracy in these systems: accidental and emergent. In both cases, the use of high-precision numerics is found to overcome any instabilities associated with biorthonormalization [52].

Another key aspect of the NRG procedure that must be adapted is the Fock-space truncation at each step. In Hermitian NRG, where the eigenvalues E_N are real, we retain only the N_k lowest-lying eigenvalues, but this becomes ambiguous in the NH context when the eigenvalues are complex. We found that truncating by the lowest real part of the eigenvalues gives the most accurate and stable results. We therefore identify the "ground state" as the one with the lowest real part (consistent with existing conventions in NH physics).

We have confirmed explicitly that applying NH-NRG to a noninteracting NH resonant level model using this truncation scheme perfectly reproduces the results of exact diagonalization, as shown in the End Matter. This provides a stringent test of the NH-NRG algorithm, which gives accurate results in the nonperturbative regime and far from the Hermitian limit. One can also check convergence upon taking $\Lambda \to 1$ [52].

Our NH-NRG code is available open source to facilitate future studies of NH quantum impurity models; see [58].

Solution of the NH Kondo model—We now apply NH-NRG to the metallic NH Kondo model (bandwidth $D \equiv 1$ hereafter). The phase diagram for antiferromagnetic $J_R > 0$ obtained by NH-NRG is presented in Fig. 1(a) as a function of the real and imaginary parts of the complex Kondo coupling, J_R and J_I. We find two phases, described by the SC and LM fixed points of the Hermitian Kondo model, separated by a quantum phase transition. We identify the phases from the NH-NRG eigenspectrum at large N after convergence, which takes a distinct form in SC and LM phases. In particular, the imaginary part of the eigenvalues $\mathrm{Im}(E_N)$ vanishes in all cases at large N, indicating the emergent Hermiticity of the fixed point Hamiltonian. Since the fixed points are Hermitian, we can compute their thermodynamic properties in the usual way [46]. As expected, we find an impurity contribution to entropy of $k_B \ln(2)$ for a free spin in the LM phase, and 0 for the screened Kondo singlet in the SC phase.

At relatively weak bare coupling $|J| \lesssim 0.25$, the NH-NRG phase boundary (black line) matches precisely with the Bethe ansatz prediction of Ref. [25], plotted as the red dot-dashed line (see inset). However at stronger coupling we find new features. For $J_R \gtrsim 0.55$ the LM phase disappears, and the Kondo effect dominates over dissipative effects. For $J_R \lesssim 0.55$ we find reentrant Kondo physics as $|J_I|$ is increased. Therefore, the dissipation-induced unscreened phase in fact occupies a bounded region in the parameter space of the NH Kondo model. Interestingly, similar phase diagrams have been observed in other non-Hermitian many-body systems [59–61].

The reentrant SC behavior at large J_I can be understood physically as a dissipation-induced localization at both the impurity site and the local bath site $f_{0\sigma}$. This state is continuously connected to the regular Hermitian Kondo-singlet fixed point at $J_I = 0$, both of which confer a $\pi/2$ scattering phase shift to bath electrons [52].

We analyze the RG flow in Figs. 1(b)–1(e) by tracking the (rescaled) NRG eigenvalues E_N as a function of iteration number N. In (b) we plot the real and imaginary parts (top and bottom panels) for a system in the SC phase, and observe clear RG flow between LM and SC fixed points. Although the imaginary part of E_N is finite for early iterations and initially grows, it decays to zero as the stable

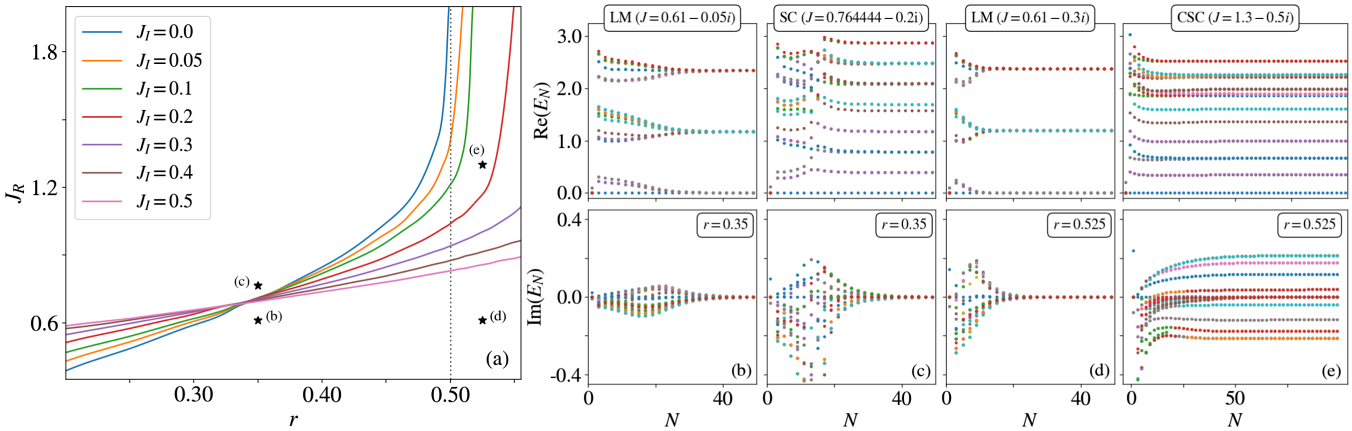

FIG. 2. Non-Hermitian pseudogap Kondo model. (a) Critical J_R separating LM and SC phases, vs pseudogap exponent r, for different J_I. Lower-critical dimension of the Hermitian model at $r = 0.5$ shown as the dotted vertical line. (b)–(e) Eigenvalue RG flow for systems indicated by the star points in (a). (b),(c) Representative LM and SC flows for $r = 0.35$. (d),(e) Flow for LM and a new "complex strong coupling" fixed point for $r = 0.525$. NH-NRG calculations with $\Lambda = 3$ and $N_k = 400$.

fixed point is reached. Interestingly, $\mathrm{Im}(E_N)$ becomes large along the crossover between fixed points. The crossover at N_c between LM and SC can be interpreted as a "temperature" scale $T_K \sim D\Lambda^{-N_c/2}$ corresponding to Kondo screening, and we numerically extract the relation $T_K \sim De^{-2DJ_R/|J|^2}$ from the NH-NRG data in the weak-coupling regime [52], consistent with the perturbative scaling result of Ref. [25].

Figure 1(c) shows the analogous plots for a system in the LM phase, which starts off close to the LM fixed point, evolves under RG, but then returns back to it at large N. This anomalous RG-flow reversion, identified in Ref. [25], is further illustrated in panels (d),(e), which show the evolution of two particular eigenvalues in the Argand plane, with increasing N following the direction of the arrows. Green points show the fixed point eigenvalues of the Hermitian Kondo model to which they converge.

The phase transition is controlled by a non-Hermitian critical fixed point [52]. At the critical point $J = J_c$, $\mathrm{Im}(E_N)$ diverges exponentially with N. Near the critical point, we identify a scale that vanishes as $T^* \sim |J - J_c|$.

NH pseudogap Kondo—To further showcase the versatility of the NH-NRG method, we now turn to the NH pseudogap Kondo model. The pseudogap bath is characterized by a density of states $\rho(\omega) = \rho_0|\omega|^r\Theta(D - |\omega|)$ with power-law exponent $r > 0$, and we focus on the particle-hole symmetric case. The standard Hermitian version of the model has been extensively studied using a variety of methods, including perturbative RG [51,62] and NRG [63,64]. A transition between LM and SC phases upon increasing J_R through the critical value $J_R^*(r)$ was found for $0 < r < \frac{1}{2}$, with $r = \frac{1}{2}$ itself playing the role of a lower-critical dimension r_c, beyond which the critical point disappears and Kondo screening is no longer possible [51]. By contrast, for the NH variant with $J \in \mathbb{C}$ we find that $r_c \equiv r_c(J_I)$ gets shifted to larger values as J_I increases. Figure 2(a) shows the phase transition boundaries obtained from NH-NRG as a function of J_R and r for different J_I. The blue line is for the Hermitian case with $J_I = 0$, which is seen to diverge at $r_c(0) = \frac{1}{2}$ as expected from Ref. [63]. For $J_I > 0$ and $0 < r < \frac{1}{2}$ our analysis of the eigenvalue RG flow shows that the stable fixed points obtained at large N are identical to the Hermitian pseudogap Kondo fixed points. Figure 2 shows the flow diagrams for $J_R < J_R^*$ in the LM phase [panel (b)] and for $J_R > J_R^*$ in the SC phase [(c)]. Likewise, the LM phase for $r > \frac{1}{2}$ in panel (d) shows RG flow to the standard Hermitian LM fixed point. However, in the region $r > \frac{1}{2}$ and $J_R > J_R^*$ that would be forbidden in the Hermitian limit, we find an entirely novel stable fixed point; see panel (e). Remarkably, in this phase the stable fixed point is intrinsically non-Hermitian, with a persistent complex eigenspectrum and $\mathrm{Im}(E_N)$ that do not decay with N. We dub this fixed point "complex strong coupling." We leave the detailed study of this phase to future work. This behavior and the structure of the full phase diagram is beyond the reach of perturbative techniques [30] or methods relying on linear dispersion.

Non-Hermitian Anderson model—Finally, we consider the physics of the NH Anderson impurity model (AIM),

$$\hat{H}_{\mathrm{AIM}} = \hat{H}_{\mathrm{bath}} + \epsilon_d \sum_\sigma d_\sigma^\dagger d_\sigma + U_d d_\uparrow^\dagger d_\uparrow d_\downarrow^\dagger d_\downarrow + V \sum_\sigma (d_\sigma^\dagger c_{0\sigma} + c_{0\sigma}^\dagger d_\sigma), \quad (2)$$

where the first line describes the isolated bath and impurity orbital, while the tunnel coupling between them is given in the second line. Non-Hermiticity can be introduced by making any or all of the parameters ϵ_d, U_d, or V complex. We focus here on the case where $V \in \mathbb{C}$ and the bath has a flat density of states. Various aspects of Anderson models describing loss and dephasing have been considered before

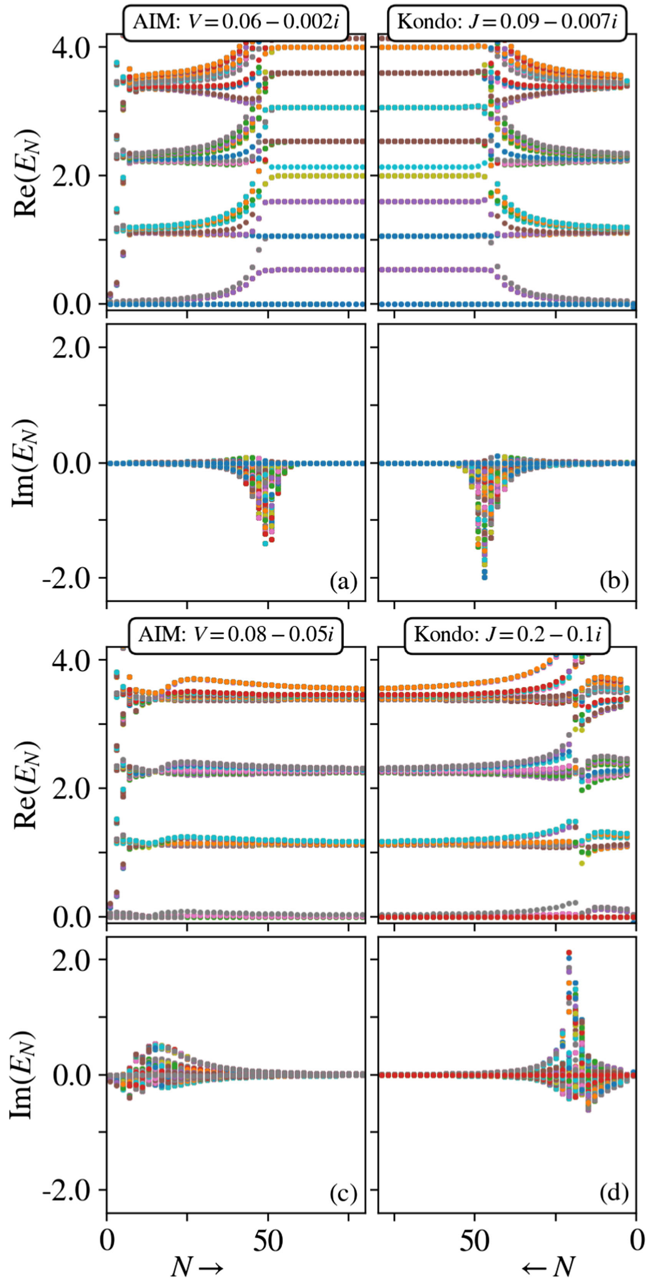

FIG. 3. Comparison of eigenvalue RG flows for NH AIM (left) and NH Kondo (right). (a),(b) Convergence to the same SC fixed point; (c),(d) convergence to the LM fixed point. NH-NRG calculations for $U_d = 0.3$, $\epsilon_d = -0.15$, $\Lambda = 3$, $N_k = 400$.

[31–34,36], but our aim here is to confirm the mapping between NH AIM and Kondo models. The Schrieffer-Wolff transformation [24,31,36] is perturbative and applies strictly only in the limit of large U_d (and therefore small J). Is the "low-energy" physics, and especially the ground state, of the AIM described by the Kondo model beyond the perturbative regime? Is the phase diagram of the NH Kondo model shown in Fig. 1(a) accessible within the AIM?

We answer these questions using nonperturbative NH-NRG. The mapping between Hermitian AIM and Kondo models beyond Schrieffer-Wolff was first established in Ref. [65] using NRG, and we adopt the same strategy here for the NH case. In Fig. 3 we confirm explicitly that the same stable fixed points are reached in the same way under RG in both models, for both SC and LM phases [66]. NH-NRG results show that the phase diagram of the NH AIM in the $(\mathrm{Re}V, \mathrm{Im}\,V)$ plane has the same structure as that of the NH Kondo model, including the reentrant Kondo behavior at large $\mathrm{Im}\,V$ [52] and termination of the LM phase beyond a critical value of $\mathrm{Re}V$. Ferromagnetic $J_R < 0$ is not accessible in the NH Kondo model.

The LM phase requires finite U_d to be stabilized: it is found to shrink upon decreasing U_d, and vanishes altogether below some finite U_d^* [52]. The SC phase of the NH AIM, realized at either small or large $\mathrm{Im}\,V$, is therefore continuously connected to the noninteracting limit $U_d \to 0$, and has a Fermi-liquid type description.

Conclusion and outlook—The numerical renormalization group is often considered the gold-standard method of choice for solving quantum impurity models [47]. Here, we generalized the method to treat non-Hermitian impurity problems, and applied our NH-NRG approach to the NH Kondo and NH Anderson models. NH-NRG is nonperturbative and can be applied equally well to nonintegrable systems and those without the linear dispersion property, such as the pseudogap Kondo model. The method provides direct access to the RG flow of the complex many-particle eigenvalues: it allows different phases to be fingerprinted by identification of characteristic fixed point structures, and emergent energy scales can be read off from the crossovers between fixed points.

NH-NRG opens the door to studying the interplay between NH and strong-correlation physics in a wide range of models—for example systems with multiple impurities [67–71] and/or multiple baths [72–75], impurities in unconventional materials [76–83], underscreened Kondo effects with higher spin [84,85], and critical phenomena near impurity quantum phase transitions [86,87]. NH-NRG could be extended to compute static physical quantities such as the impurity magnetization [52], and zero-temperature dynamical quantities such as the impurity spectral function [55]. This would allow non-Hermitian lattice models [88,89] to be studied within dynamical mean-field theory [90], using NH-NRG as an impurity solver. Our NH-NRG code is provided open source at Ref. [58].

Acknowledgments—The authors acknowledge funding from Taighde Éireann—Research Ireland through Grant No. 21/RP-2TF/10019. We are grateful to Ralph Smith for providing the "GenericSchur" Julia package [91].

Data availability—The data that support the findings of this article are not publicly available upon publication because it is not technically feasible and/or the cost of preparing, depositing, and hosting the data would be prohibitive within the terms of this research project. The data are available from the authors upon reasonable request.

[1] I. Rotter, A non-Hermitian Hamilton operator and the physics of open quantum systems, J. Phys. A **42**, 153001 (2009).

[2] F. Minganti, A. Miranowicz, R. W. Chhajlany, and F. Nori, Quantum exceptional points of non-Hermitian Hamiltonians and Liouvillians: The effects of quantum jumps, Phys. Rev. A **100**, 062131 (2019).

[3] Y. Ashida, Z. Gong, and M. Ueda, Non-Hermitian physics, Adv. Phys. **69**, 249 (2020).

[4] E. J. Bergholtz, J. C. Budich, and F. K. Kunst, Exceptional topology of non-Hermitian systems, Rev. Mod. Phys. **93**, 015005 (2021).

[5] F. Roccati, G. M. Palma, F. Ciccarello, and F. Bagarello, Non-Hermitian physics and master equations, Open Syst. Inf. Dyn. **29**, 2250004 (2022).

[6] D. C. Brody, Biorthogonal quantum mechanics, J. Phys. A **47**, 035305 (2013).

[7] J. Wiersig, Role of nonorthogonality of energy eigenstates in quantum systems with localized losses, Phys. Rev. A **98**, 052105 (2018).

[8] W. D. Heiss and A. L. Sannino, Avoided level crossing and exceptional points, J. Phys. A **23**, 1167 (1990).

[9] W. Heiss and H. Harney, The chirality of exceptional points, Eur. Phys. J. D **17**, 149 (2001).

[10] M. Berry, Physics of non-Hermitian degeneracies, Czech. J. Phys. **54**, 1039 (2004).

[11] M. Müller and I. Rotter, Exceptional points in open quantum systems, J. Phys. A **41**, 244018 (2008).

[12] W. D. Heiss, The physics of exceptional points, J. Phys. A **45**, 444016 (2012).

[13] P. C. Burke, J. Wiersig, and M. Haque, Non-Hermitian scattering on a tight-binding lattice, Phys. Rev. A **102**, 012212 (2020).

[14] S. Sayyad, M. Stålhammar, L. Rødland, and F. K. Kunst, Symmetry-protected exceptional and nodal points in non-Hermitian systems, SciPost Phys. **15**, 200 (2023).

[15] Z.-J. Li, G. Cardoso, E. J. Bergholtz, and Q.-D. Jiang, Braids and higher-order exceptional points from the interplay between lossy defects and topological boundary states, Phys. Rev. Res. **6**, 043023 (2024).

[16] A. Montag and F. K. Kunst, Symmetry-induced higher-order exceptional points in two dimensions, Phys. Rev. Res. **6**, 023205 (2024).

[17] Y. H. Erdogan and M. Haque, Supercharging exceptional points: Full-spectrum pairwise coalescence in non-Hermitian systems, arXiv:2411.06305.

[18] J. T. Gohsrich, J. Fauman, and F. K. Kunst, Exceptional points of any order in a generalized Hatano-Nelson model, arXiv:2403.12018.

[19] C. M. Bender and S. Boettcher, Real spectra in non-Hermitian Hamiltonians having $\mathcal{PT}$-symmetry, Phys. Rev. Lett. **80**, 5243 (1998).

[20] C. M. Bender, D. C. Brody, and H. F. Jones, Complex extension of quantum mechanics, Phys. Rev. Lett. **89**, 270401 (2002).

[21] C. M. Bender, Making sense of non-Hermitian Hamiltonians, Rep. Prog. Phys. **70**, 947 (2007).

[22] P. Zhong, W. Pan, H. Lin, X. Wang, and S. Hu, Density-matrix renormalization group algorithm for non-Hermitian systems, Phys. Rev. Lett. **135**, 106502 (2025).

[23] Y.-Y. Fang, Z.-Y. Zhang, C. Sun, X.-Y. Xu, and J.-M. Liu, Exploring tunable non-Hermitian spin models based on dissipative bosonic atoms, Phys. Rev. B **111**, 054444 (2025).

[24] A. C. Hewson, *The Kondo Problem to Heavy Fermions* (Cambridge University Press, Cambridge, England, 1993).

[25] M. Nakagawa, N. Kawakami, and M. Ueda, Non-Hermitian Kondo effect in ultracold alkaline-earth atoms, Phys. Rev. Lett. **121**, 203001 (2018).

[26] M. Hasegawa, M. Nakagawa, and K. Saito, Kondo effect in a quantum dot under continuous quantum measurement, arXiv:2111.07771.

[27] S. Han, D. J. Schultz, and Y. B. Kim, Complex fixed points of the non-Hermitian Kondo model in a Luttinger liquid, Phys. Rev. B **107**, 235153 (2023).

[28] P. Kattel, A. Zhakenov, P. R. Pasnoori, P. Azaria, and N. Andrei, Dissipation driven phase transition in the non-Hermitian Kondo model, Phys. Rev. B **111**, L201106 (2025).

[29] P. Kattel, P. R. Pasnoori, J. H. Pixley, and N. Andrei, Spin chain with non-Hermitian $\mathcal{PT}$-symmetric boundary couplings: Exact solution, dissipative Kondo effect, and phase transitions on the edge, Phys. Rev. B **111**, 224407 (2025).

[30] J. Chen, Critical behavior of non-Hermitian Kondo effect in pseudogap system, arXiv:2403.17586.

[31] J. A. S. Lourenço, R. L. Eneias, and R. G. Pereira, Kondo effect in a $\mathcal{PT}$-symmetric non-Hermitian Hamiltonian, Phys. Rev. B **98**, 085126 (2018).

[32] V. M. Kulkarni, A. Gupta, and N. S. Vidhyadhiraja, Kondo effect in a non-Hermitian $\mathcal{PT}$-symmetric Anderson model with Rashba spin-orbit coupling, Phys. Rev. B **106**, 075113 (2022).

[33] K. Yamamoto, M. Nakagawa, and N. Kawakami, Correlation versus dissipation in a non-Hermitian Anderson impurity model, Phys. Rev. B **111**, 125157 (2025).

[34] V. M. Kulkarni and N. Vidhyadhiraja, Anderson impurities in edge states with nonlinear and dissipative perturbations, SciPost Phys. **19**, 036 (2025).

[35] T. Yoshimura, K. Bidzhiev, and H. Saleur, Non-Hermitian quantum impurity systems in and out of equilibrium: Noninteracting case, Phys. Rev. B **102**, 125124 (2020).

[36] M. Vanhoecke and M. Schirò, Kondo-Zeno crossover in the dynamics of a monitored quantum dot, Nat. Commun. **16**, 6155 (2025).

[37] M. Vanhoecke, N. Tsuji, and M. Schirò, Dissipative Kondo physics in the Anderson impurity model with two-body losses, arXiv:2506.22302.

[38] D. Werner, M. Vanhoecke, M. Schirò, and E. Arrigoni, Nonequilibrium transport through an interacting monitored quantum dot, arXiv:2507.20779.

[39] A. Picano, M. Vanhoecke, and M. Schirò, Heating dynamics of correlated Fermions under dephasing, arXiv:2507.21804.

[40] M. Stefanini, Y.-F. Qu, T. Esslinger, S. Gopalakrishnan, E. Demler, and J. Marino, Dissipative realization of Kondo models, Commun. Phys. **8**, 212 (2025).
[41] Y.-F. Qu, M. Stefanini, T. Shi, T. Esslinger, S. Gopalakrishnan, J. Marino, and E. Demler, Variational approach to the dynamics of dissipative quantum impurity models, Phys. Rev. B **111**, 155113 (2025).
[42] E. S. Sørensen and I. Affleck, Scaling theory of the Kondo screening cloud, Phys. Rev. B **53**, 9153 (1996).
[43] A. K. Mitchell, M. Becker, and R. Bulla, Real-space renormalization group flow in quantum impurity systems: Local moment formation and the Kondo screening cloud, Phys. Rev. B **84**, 115120 (2011).
[44] S.-S. B. Lee, J. Park, and H.-S. Sim, Macroscopic quantum entanglement of a Kondo cloud at finite temperature, Phys. Rev. Lett. **114**, 057203 (2015).
[45] P. W. Anderson, A poor man's derivation of scaling laws for the Kondo problem, J. Phys. C **3**, 2436 (1970).
[46] K. G. Wilson, The renormalization group: Critical phenomena and the Kondo problem, Rev. Mod. Phys. **47**, 773 (1975).
[47] R. Bulla, T. A. Costi, and T. Pruschke, Numerical renormalization group method for quantum impurity systems, Rev. Mod. Phys. **80**, 395 (2008).
[48] N. Andrei, K. Furuya, and J. H. Lowenstein, Solution of the Kondo problem, Rev. Mod. Phys. **55**, 331 (1983).
[49] N. Syassen, D. M. Bauer, M. Lettner, T. Volz, D. Dietze, J. J. García-Ripoll, J. I. Cirac, G. Rempe, and S. Dürr, Strong dissipation inhibits losses and induces correlations in cold molecular gases, Science **320**, 1329 (2008).
[50] I. Affleck and A. W. W. Ludwig, Universal noninteger "ground-state degeneracy" in critical quantum systems, Phys. Rev. Lett. **67**, 161 (1991).
[51] L. Fritz and M. Vojta, Phase transitions in the pseudogap Anderson and Kondo models: Critical dimensions, renormalization group, and local-moment criticality, Phys. Rev. B **70**, 214427 (2004).
[52] See Supplemental Material at http://link.aps.org/supplemental/10.1103/19td-1k9s for further details of (i) NH matrix properties, (ii) derivation of iterative diagonalization procedure in NH-NRG, (iii) alternative truncation schemes, (iv) additional examples of RG flows for the NH AIM, (v) evolution of the Kondo temperature, (vi) properties of the critical point, (vii) interpretation of reentrant SC behavior, (viii) convergence of NH-NRG results with Λ, and (ix) ground state impurity magnetization data.
[53] The spin density of the discretized bath at the impurity position is $\hat{\boldsymbol{S}}_0 = \frac{1}{2}\sum_{\sigma,\sigma'} f^{\dagger}_{0\sigma}\boldsymbol{\tau}_{\sigma,\sigma'} f_{0\sigma'}$.
[54] Non-Abelian symmetries can also be leveraged to diagonalize the Hamiltonian in multiplet space [55].
[55] A. Weichselbaum and J. von Delft, Sum-rule conserving spectral functions from the numerical renormalization group, Phys. Rev. Lett. **99**, 076402 (2007).
[56] S.-S. B. Lee and A. Weichselbaum, Adaptive broadening to improve spectral resolution in the numerical renormalization group, Phys. Rev. B **94**, 235127 (2016).
[57] A. Weichselbaum, Non-abelian symmetries in tensor networks: A quantum symmetry space approach, Ann. Phys. (Amsterdam) **327**, 2972 (2012).
[58] P. C. Burke and A. K. Mitchell, https://github.com/PhillipBC/NonHermitianNRG (Non-Hermitian NRG GitHub).
[59] K. Yamamoto, M. Nakagawa, K. Adachi, K. Takasan, M. Ueda, and N. Kawakami, Theory of non-Hermitian fermionic superfluidity with a complex-valued interaction, Phys. Rev. Lett. **123**, 123601 (2019).
[60] M. Nakagawa, N. Kawakami, and M. Ueda, Exact Liouvillian spectrum of a one-dimensional dissipative Hubbard model, Phys. Rev. Lett. **126**, 110404 (2021).
[61] H. Li, X.-H. Yu, M. Nakagawa, and M. Ueda, Yang-Lee zeros, semicircle theorem, and nonunitary criticality in Bardeen-Cooper-Schrieffer superconductivity, Phys. Rev. Lett. **131**, 216001 (2023).
[62] L. Fritz, S. Florens, and M. Vojta, Universal crossovers and critical dynamics of quantum phase transitions: A renormalization group study of the pseudogap Kondo problem, Phys. Rev. B **74**, 144410 (2006).
[63] R. Bulla, T. Pruschke, and A. C. Hewson, Anderson impurity in pseudo-gap Fermi systems, J. Phys. Condens. Matter **9**, 10463 (1997).
[64] C. Gonzalez-Buxton and K. Ingersent, Renormalization-group study of Anderson and Kondo impurities in gapless Fermi systems, Phys. Rev. B **57**, 14254 (1998).
[65] H. Krishna-murthy, J. Wilkins, and K. Wilson, Renormalization-group approach to the Anderson model of dilute magnetic alloys. I. Static properties for the symmetric case, Phys. Rev. B **21**, 1003 (1980).
[66] Note that the initial flow for the AIM is expected to be different from that of the Kondo model because of the existence of the additional "free orbital" fixed point in the UV.
[67] I. Affleck, A. W. W. Ludwig, and B. A. Jones, Conformal-field-theory approach to the two-impurity Kondo problem: Comparison with numerical renormalization-group results, Phys. Rev. B **52**, 9528 (1995).
[68] A. Allerdt, C. A. Büsser, G. B. Martins, and A. E. Feiguin, Kondo versus indirect exchange: Role of lattice and actual range of RKKY interactions in real materials, Phys. Rev. B **91**, 085101 (2015).
[69] A. K. Mitchell, T. F. Jarrold, and D. E. Logan, Quantum phase transition in quantum dot trimers, Phys. Rev. B **79**, 085124 (2009).
[70] R. Žitko and J. Bonča, Multiple-impurity Anderson model for quantum dots coupled in parallel, Phys. Rev. B **74**, 045312 (2006).
[71] D. B. Karki, E. Boulat, W. Pouse, D. Goldhaber-Gordon, A. K. Mitchell, and C. Mora, $\mathbb{Z}_3$ Parafermion in the double charge Kondo model, Phys. Rev. Lett. **130**, 146201 (2023).
[72] P. Nozières and A. Blandin, Kondo effect in real metals, J. Phys. (Paris) **41**, 193 (1980).
[73] A. Tóth, L. Borda, J. Von Delft, and G. Zaránd, Dynamical conductance in the two-channel Kondo regime of a double dot system, Phys. Rev. B **76**, 155318 (2007).
[74] Z. Iftikhar, A. Anthore, A. Mitchell, F. Parmentier, U. Gennser, A. Ouerghi, A. Cavanna, C. Mora, P. Simon, and F. Pierre, Tunable quantum criticality and super-ballistic transport in a "charge" Kondo circuit, Science **360**, 1315 (2018).

[75] A. K. Mitchell, E. Sela, and D. E. Logan, Two-channel Kondo physics in two-impurity Kondo models, Phys. Rev. Lett. **108**, 086405 (2012).

[76] L. Fritz and M. Vojta, The physics of Kondo impurities in graphene, Rep. Prog. Phys. **76**, 032501 (2013).

[77] A. K. Mitchell and L. Fritz, Kondo effect with diverging hybridization: Possible realization in graphene with vacancies, Phys. Rev. B **88**, 075104 (2013).

[78] A. S. Shankar, D. O. Oriekhov, A. K. Mitchell, and L. Fritz, Kondo effect in twisted bilayer graphene, Phys. Rev. B **107**, 245102 (2023).

[79] A. K. Mitchell, D. Schuricht, M. Vojta, and L. Fritz, Kondo effect on the surface of three-dimensional topological insulators: Signatures in scanning tunneling spectroscopy, Phys. Rev. B **87**, 075430 (2013).

[80] A. K. Mitchell and L. Fritz, Kondo effect in three-dimensional Dirac and Weyl systems, Phys. Rev. B **92**, 121109 (2015).

[81] M. R. Galpin and D. E. Logan, Anderson impurity model in a semiconductor, Phys. Rev. B **77**, 195108 (2008).

[82] C. P. Moca, I. Weymann, M. A. Werner, and G. Zaránd, Kondo cloud in a superconductor, Phys. Rev. Lett. **127**, 186804 (2021).

[83] M. Vojta, A. K. Mitchell, and F. Zschocke, Kondo impurities in the Kitaev spin liquid: Numerical renormalization group solution and gauge-flux-driven screening, Phys. Rev. Lett. **117**, 037202 (2016).

[84] J. J. Parks, A. R. Champagne, T. A. Costi, W. W. Shum, A. N. Pasupathy, E. Neuscamman, S. Flores-Torres, P. S. Cornaglia, A. A. Aligia, C. A. Balseiro, G. K.-L. Chan, H. D. Abruña, and D. C. Ralph, Mechanical control of spin states in spin-1 molecules and the underscreened Kondo effect, Science **328**, 1370 (2010).

[85] P. Mehta, N. Andrei, P. Coleman, L. Borda, and G. Zarand, Regular and singular Fermi-liquid fixed points in quantum impurity models, Phys. Rev. B **72**, 014430 (2005).

[86] I. Affleck and A. W. Ludwig, Critical theory of overscreened Kondo fixed points, Nucl. Phys. **B360**, 641 (1991).

[87] M. Vojta, Impurity quantum phase transitions, Philos. Mag. **86**, 1807 (2006).

[88] T. Fukui and N. Kawakami, Breakdown of the Mott insulator: Exact solution of an asymmetric Hubbard model, Phys. Rev. B **58**, 16051 (1998).

[89] T. Hayata and A. Yamamoto, Non-Hermitian Hubbard model without the sign problem, Phys. Rev. B **104**, 125102 (2021).

[90] A. Georges, G. Kotliar, W. Krauth, and M. J. Rozenberg, Dynamical mean-field theory of strongly correlated fermion systems and the limit of infinite dimensions, Rev. Mod. Phys. **68**, 13 (1996).

[91] R. Smith, https://github.com/ralphas/genericschur.jl (GenericSchur Julia library).

End Matter

Iterative diagonalization—Here, we give an overview of the NH-NRG algorithm, highlighting key differences with the Hermitian formulation described in Ref. [47]. In the following we assume a biorthonormal basis [6] such that the inner product of left and right states satisfies $\langle n|m\rangle^{L,R} = \delta_{nm}$. Further details can be found in Supplemental Material [52].

At step $N+1$ of the NH-NRG calculation, we construct the Hamiltonian matrix $\mathbf{H}^b_{N+1}$ with elements

$$\langle N+1;k;r|^L_b \hat{H}_{N+1}|N+1;k';r'\rangle^R_b, \tag{A1}$$

where $L(R)$ refers to the left(right) states, and the b subscript denotes the basis states, which are decomposed as

$$|N+1;k;r\rangle^{L(R)}_b = |k\rangle_{N+1} \otimes |N;r\rangle^{L(R)}_d. \tag{A2}$$

Here, $|N;r\rangle^{L(R)}_d$ are the N_k retained left(right) eigenstates of the previous iteration satisfying $\hat{H}_N|N;r\rangle^R_d = E_N(r)|N;r\rangle^R_d$ and $\langle N;r|^L_d \hat{H}_N = \langle N;r|^L_d E_N(r)$, whereas $|k\rangle_{N+1} = \{|-\rangle, |\downarrow\rangle, |\uparrow\rangle, |\uparrow\downarrow\rangle\}$ are the four states of the added orbital $N+1$, labeled respectively by the index $k = \{0,-1,+1,2\}$, which are equal for L and R.

From the recursion relation $\hat{H}_{N+1} = \hat{H}_N + \hat{T}_{N+1}$ and Eq. (A2), we may then express the matrix elements as

$$\begin{aligned}
&\langle N+1;k;r|^L_b \hat{H}_{N+1}|N+1;k';r'\rangle^R_b \\
&= \langle k|_{N+1}\langle N;r|^L_d \hat{H}_N|k'\rangle_{N+1}|N;r'\rangle^R_d \\
&\quad + \epsilon_{N+1}\sum_\sigma \langle k|_{N+1}\langle N;r|^L_d f^\dagger_{N+1\sigma}f_{N+1\sigma}|k'\rangle_{N+1}|N;r'\rangle^R_d \\
&\quad + t_N\sum_\sigma \langle k|_{N+1}\langle N;r|^L_d f^\dagger_{N\sigma}f_{N+1\sigma}|k'\rangle_{N+1}|N;r'\rangle^R_d \\
&\quad + t_N\sum_\sigma \langle k|_{N+1}\langle N;r|^L_d f^\dagger_{N+1\sigma}f_{N\sigma}|k'\rangle_{N+1}|N;r'\rangle^R_d.
\end{aligned} \tag{A3}$$

This expression simplifies to

$$\begin{aligned}
&\langle N+1;k;r|^L_b \hat{H}_{N+1}|N+1;k';r'\rangle^R_b \\
&= \delta_{kk'}\delta_{rr'}(E_N(r) + |k|\epsilon_{N+1}) \\
&\quad + (-1)^k t_N \sum_\sigma M^\sigma_{kk'}\langle N;r|^L_d f^\dagger_{N\sigma}|N;r'\rangle^R_d \\
&\quad + (-1)^{k'} t_N \sum_\sigma M^\sigma_{k'k}\langle N;r|^L_d f_{N\sigma}|N;r'\rangle^R_d,
\end{aligned} \tag{A4}$$

where in the last two lines we inserted the identity between the creation and annihilation operators [52]. Here, $M^\sigma_{kk'} = (M^\sigma_{k'k})^\dagger$ denotes the trivial matrix element $\langle k|f_{N+1\sigma}|k'\rangle_{N+1}$ whose value does not depend on N.

Thus we can construct the Hamiltonian matrix $\mathbf{H}^b_{N+1}$ at NRG iteration $N+1$ using information from iteration N.

Specifically, we need the set of complex eigenvalues $E_N(r)$, and the matrix elements $\langle N;r|_d^L f_{N\sigma}^\dagger|N;r'\rangle_d^R$ and $\langle N;r|_d^L f_{N\sigma}|N;r'\rangle_d^R$, which in the NH case are *not* Hermitian conjugates and need to be computed separately.

With $\mathbf{H}_{N+1}^b$ in hand, we diagonalize the matrix to obtain the eigenvalues E_{N+1} and the left and right eigenvectors $|N+1;r\rangle_d^{L(R)}$. Specifically, $\mathbf{H}_{N+1}^b = \mathbf{U}_{N+1}^R \mathbf{H}_{N+1}^d (\mathbf{U}_{N+1}^L)^\dagger$ where $\mathbf{H}_{N+1}^d$ is the diagonal matrix of eigenvalues E_{N+1} and $\mathbf{U}_{N+1}^{R(L)}$ is a matrix whose columns are the right(left) eigenvectors. Therefore we can expand the eigenstates as

$$\begin{aligned}|N+1;r\rangle_d^{R(L)} &= \sum_{m,s} U_{N+1}^{R(L)}(r;m,s)^{(\dagger)}|N+1;m;s\rangle_b^{R(L)} \\ &\equiv \sum_{m,s} U_{N+1}^{R(L)}(r;m,s)^{(\dagger)}|m\rangle_{N+1}|N;s\rangle_d^{R(L)}.\end{aligned} \tag{A5}$$

We use this to construct the nontrivial matrix elements required for the next step,

$$\begin{aligned}&\langle N+1;r|_d^L f_{N+1\sigma}^\dagger|N+1;r'\rangle_d^R \\ &\quad= \sum_{m,m',s} M_{m'm}^\sigma U_{N+1}^L(r;m,s)^\dagger U_{N+1}^R(r';m',s)\end{aligned} \tag{A6}$$

$$\begin{aligned}&\langle N+1;r|_d^L f_{N+1\sigma}|N+1;r'\rangle_d^R \\ &\quad= \sum_{m,m',s} M_{mm'}^\sigma U_{N+1}^L(r;m,s)^\dagger U_{N+1}^R(r';m',s).\end{aligned} \tag{A7}$$

Note that only the "lowest" N_k eigenstates are retained at each step, meaning that the computational complexity is approximately constant at each step. In practice this Fock space truncation is done by retaining states with the lowest real part of the complex eigenvalues E_N.

As such, the chain can be built up iteratively, starting from $\hat{H}_0$ consisting of just the impurity and the Wilson zero orbital. Since states with large $\mathrm{Re}(E_N)$ are discarded at each step, we focus on the states with progressively smaller $\mathrm{Re}(E_N)$ as the calculation proceeds. To analyze the RG flow we specify E_N with respect to the state with the lowest $\mathrm{Re}(E_N)$ at that iteration, and rescale by a factor of $\Lambda^{N/2}$. It is these rescaled eigenvalues that are plotted in the figures.

Truncation schemes and numerical precision—Through extensive numerical testing, we found that truncation to the N_k states with the lowest $\mathrm{Re}(E_N)$ at each step yields the most stable and accurate results. In this Letter we presented results for $\Lambda = 3$ and $N_k = 400$, which we explicitly checked were numerically converged with respect to increasing N_k (essentially no change in the RG flow was observed by increasing N_k to 1024 kept states). In certain cases we observed numerical instabilities in the diagonalization that were completely resolved by using high-precision numerics. All of the results presented were confirmed to be converged using 128-bit precision complex numbers [91].

Other truncation schemes (discussed further below) were investigated. For example, truncation to the N_k states with the lowest magnitude $|E_N|$ produces a somewhat different set of states being tracked along the RG flow. However, retained states common to both truncation schemes were found to have exactly the same RG flow, provided N_k was sufficiently large. Overall, truncation by lowest $\mathrm{Re}(E_N)$ is preferred due to advantageous stability and accuracy with respect to N_k, and less frequent need for high-precision numerics.

Validation and benchmarking of method—The NH-NRG method for the AIM works with equal ease for any interaction strength U_d. In particular, the NH-NRG algorithm works exactly the same for the trivial case $U_d = 0$ as for the nontrivial interacting case with $U_d > 0$. For $U_d = 0$ we can also simply diagonalize the single-particle Hamiltonian matrix and then construct the many-particle states from these. Thus in this limit we can exactly diagonalize the full impurity-and-Wilson-chain composite system without any truncation or approximation. This provides a stringent check on our NH-NRG results by direct comparison.

Our results of this testing are shown in Fig. 4 for the $U_d = 0$ AIM (also known as the resonant level model) in which a noninteracting impurity is coupled to the usual (flat-band) Wilson chain of $N+1$ sites. We compare NH-NRG results (red diamond points) with $N_k = 1024$ kept states, and exact diagonalization of the tight-binding model (black circle points). In the latter we construct the full 4^{N+2} dimensional Fock space. Complex eigenvalues of $\hat{H}_N$ are plotted for different N in the Argand plane in Fig. 4. Top row (a) shows results for the truncation scheme "LowRe" in which the N_k states with the lowest $\mathrm{Re}(E_N)$ are retained; whereas the bottom row (b) is for the "LowMag" scheme where the N_k states with the lowest $|E_N|$ are instead kept. Although a different set of states in the NH-NRG calculation is retained in either case, these accurately match with the corresponding exact diagonalization results from the tight-binding chain. We note that the NH-NRG results for $N = 5$ in panel (b) are highly degenerate, with the $N_k = 1024$ retained states giving only three distinct eigenvalues. The kept eigenvalues in (a) are far less degenerate. In the case of high degeneracy, which poses a challenge for numerical diagonalization and biorthonormalization of NH matrices, we add a physically inconsequential on-site disorder to the Wilson chain of width 10^{-7}, which lifts the degeneracy. This precaution was not required for any of the interacting models studied. Excellent agreement was also confirmed for large $\mathrm{Im}\,V$ in the nonperturbative regime far from the Hermitian limit.

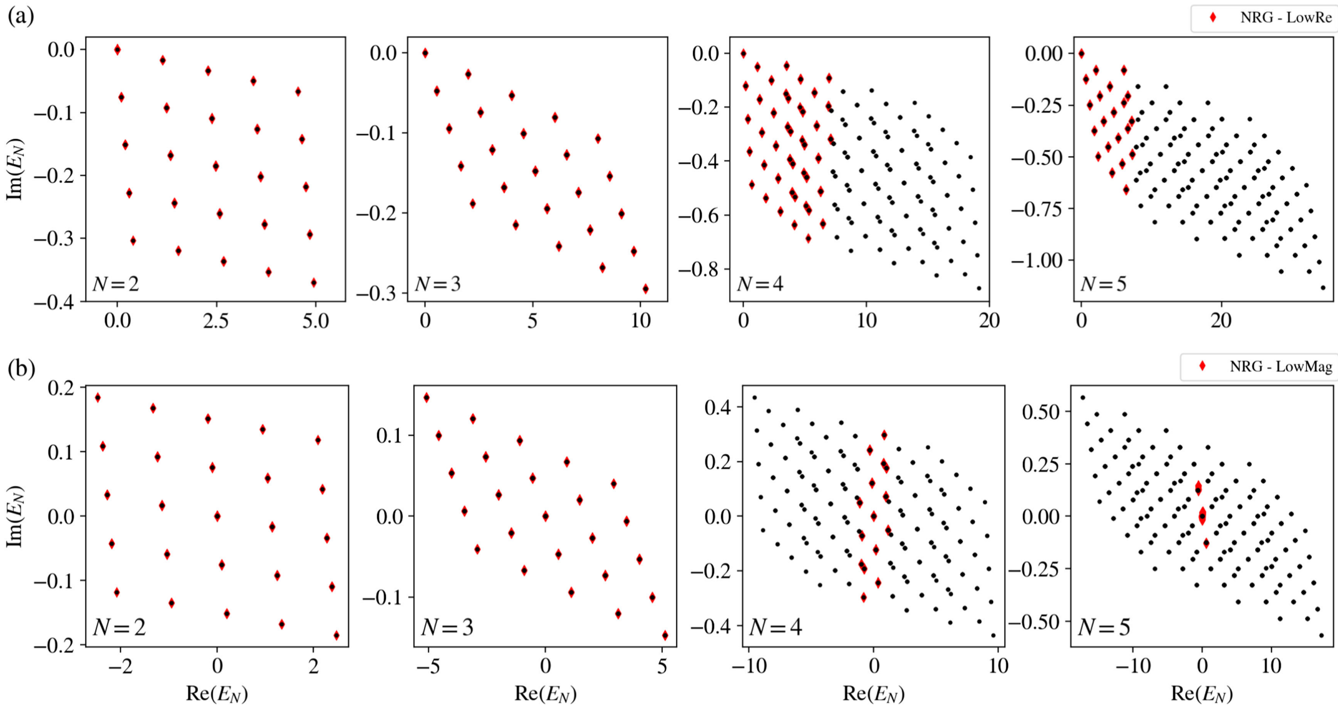

FIG. 4. Validation of NH-NRG method for the noninteracting AIM with $U_d = 0$. The full set of complex eigenvalues are constructed from exact diagonalization of $\hat{H}_N$ and shown in the Argand plane for $N = 2, 3, 4, 5$ as the black circle points. NH-NRG results are shown as the red diamond points: the $\min(N_k, 4^{N+2})$ retained states match precisely with the exact results. Top row (a) shows NH-NRG truncation scheme LowRe in which the lowest N_k states sorted by $\mathrm{Re}(E_N)$ are kept. Bottom row (b) shows an alternative truncation scheme LowMag, where states are sorted by $|E_N|$. Shown for $\Lambda = 3$, $N_k = 1024$, $\epsilon_d = 0$, $V = 0.1 - 0.08i$. Eigenvalues rescaled by $\Lambda^{N/2}$ are plotted with respect to the ground state of that iteration.

Additional examples of different truncation schemes and benchmarking for different noninteracting models are provided in Supplemental Material [52]. We have also checked that our NH-NRG code reproduces the results of standard NRG when $\hat{H}_0$ is Hermitian.

Supplemental Material for *Non-Hermitian Numerical Renormalization Group: Solution of the non-Hermitian Kondo model*

Phillip C. Burke[1,2] and Andrew K. Mitchell[1,2]
[1] *School of Physics, University College Dublin, Belfield, Dublin 4, Ireland*
[2] *Centre for Quantum Engineering, Science, and Technology, University College Dublin, Dublin 4, Ireland*

In this Supplemental Material we provide supporting information and data.

- In Section S.I, we discuss some basic properties of non-Hermitian (NH) systems.
- In Section S.II, we provide the complete derivation of the iterative construction of the Hamiltonian used in the non-Hermitian numerical renormalization group (NH-NRG) method.
- In Section S.III, we illustrate alternative truncation schemes for the NH-NRG procedure.
- In Section S.IV, we provide additional eigenvalue flow diagrams for the NH Anderson Impurity Model (AIM).
- In Section S.V, we discuss the evolution of the Kondo temperature T_K.
- In Section S.VI, we present further results for the critical point of the NH Kondo model.
- In Section S.VII, we discuss the physical interpretation of the re-entrant strong-coupling (SC) behavior.
- In Section S.VIII, we discuss convergence of NH-NRG results in the $\Lambda \to 1$ limit.
- In Section S.IX, we present some initial results for the impurity magnetization in the NH Kondo model.

S.I. NON-HERMITIAN SYSTEMS

Before jumping into the iterative construction procedure used in NH-NRG, we first provide a brief discussion of NH matrices which will come in useful later. See also Refs. [1, 2] for discussions of bi-orthogonal quantum mechanics.

For an NH system, for which $\hat{H} \neq \hat{H}^\dagger$, the left and right eigenvectors are defined such that,

$$\hat{H}\,|E_j\rangle^R = \lambda_j\,|E_j\rangle^R \quad , \quad \hat{H}^\dagger\,|E_j\rangle^L = \lambda_j^*\,|E_j\rangle^L \tag{S.1}$$

$$\langle E_j|^R\,\hat{H}^\dagger = \langle E_j|^R\,\lambda_j^* \quad , \quad \langle E_j|^L\,\hat{H} = \langle E_j|^L\,\lambda_j . \tag{S.2}$$

Although the left and right eigenvectors are not individually orthonormal, they may form a bi-orthogonal basis if the eigenspectrum is non-degenerate. In the following we assume this property, which can be defined as,

$$\langle E_i|E_j\rangle^{LR} = \delta_{ij} \; . \tag{S.3}$$

Here we have also bi-*normalized* the basis. We note that a bi-orthonormal basis is not the default output for left and right eigenvectors from most standard numerical eigensolvers (e.g. via Python, Julia, or Fortran) and so the bi-normalization typically has to be done manually.

To bi-normalize the left and right eigenvectors, we first compute the overlaps,

$$\mathrm{LR}_j = \langle E_j|E_j\rangle^{LR} \; , \tag{S.4}$$

and then, provided the corresponding left and right eigenvectors are non-orthogonal, we rescale the vectors,

$$|E_j\rangle^R \to \frac{|E_j\rangle^R}{\sqrt{\mathrm{LR_j}}} \qquad , \qquad |E_j\rangle^L \to \frac{|E_j\rangle^L}{\sqrt{\mathrm{LR_j}}^*} \; , \tag{S.5}$$

which ensures $\langle E_j|E_j\rangle^{LR} = 1$.

Assuming bi-orthonormality now, an NH matrix $\hat{H}$ can be decomposed in terms of its left and right eigenvectors,

$$\hat{H} \quad = \sum_j \lambda_j |E_j\rangle\langle E_j|^{RL} \qquad , \qquad \langle E_j|^L\,\hat{H}\,|E_k\rangle^R = \delta_{jk}\lambda_j \; . \tag{S.6}$$

With some bi-normalized basis $|\phi_j\rangle^{L(R)}$ of left(right) states, we can construct the Hamiltonian matrix $\mathbf{H}_\phi$ with elements $[\mathbf{H}_\phi]_{ij} = \langle\phi_i|^L \hat{H} |\phi_j\rangle^R$. Numerical diagonalization of this matrix yields $\mathbf{U}^R \mathbf{H}_E (\mathbf{U}^L)^\dagger = \mathbf{H}_\phi$ where $[\mathbf{H}_E]_{ij} = \delta_{ij}\lambda_j$ and the columns of the matrices $\mathbf{U}^R$ and $\mathbf{U}^L$ contain the right and left eigenvectors. It follows that,

$$(\mathbf{U}^L)^\dagger \mathbf{U}^R = \mathbf{I} \qquad ; \qquad \mathrm{tr}\big[(\mathbf{U}^L)^\dagger \mathbf{U}^R\big] = \dim(\mathbf{H}) \; . \tag{S.7}$$

However, note that $(\mathbf{U}^{L(R)})^\dagger \mathbf{U}^{L(R)} \neq \mathbf{I}$ since the left and right sets themselves are not orthonormal.

Importantly, for bi-orthonormal systems the identity can be resolved as,

$$\mathbb{1} = \sum_j |\phi_j\rangle \langle\phi_j|^{RL} \; . \tag{S.8}$$

One issue with the bi-orthonormalization procedure is that it requires a non-degenerate eigenspectrum [1]. In general, degeneracies can arise in three ways: (i) due to symmetries of the system; (ii) accidental degeneracies; and (iii) emergent degeneracies. For degeneracies due to exact symmetries of the bare Hamiltonian, the solution is to label states by their associated conserved quantum numbers and block-diagonalize the Hamiltonian separately in each quantum number subspace. A bi-orthonormal basis can then be defined separately in each block and different degenerate components of a symmetry multiplet are treated independently. For accidental degeneracies, often numerical error even at machine precision level is sufficient to distinguish states and eliminate problems with bi-orthonormalization. These issues were discussed in a different context for NRG calculations in Ref. [3]. We note that the procedure is stabilized by simply using 128-bit precision numerics, which is typically enough to distinguish accidental degeneracies, which are of course always approximate in practice. Another simple solution is to add to the Hamiltonian a physically inconsequential disorder perturbation of very small magnitude, which has the effect of lifting the degeneracies. Finally, in the context of quantum impurity problems, we note that low-energy fixed points can have larger *emergent* symmetries than the bare model Hamiltonian. For example the one-channel, spin-$\frac{1}{2}$ anisotropic Kondo model has an *isotropic* strong coupling stable fixed point [4]; whereas the two-channel Kondo model has a large emergent SO(8) symmetry at its critical point [5]. In these cases, one might expect additional degeneracies that cannot be separated into distinct quantum number blocks. However, these emergent symmetries only pertain asymptotically after very many NRG iterations, and at low energies. In practice, the degeneracies near the fixed point are always approximate and again, the use of high-precision numerics solves the problem.

S.II. ITERATIVE CONSTRUCTION AND DIAGONALIZATION IN NH-NRG

In the following we assume that left and right vectors of NH matrices are bi-orthonormal. The NRG procedure is defined by the recursion relation,

$$\hat{H}_{N+1} = \hat{H}_N + \hat{T}_{N+1} \tag{S.9}$$

which is initialized by $\hat{H}_0$, consisting of the impurity degrees of freedom and the Wilson chain 'zero' orbital. Here the operator $\hat{T}_{N+1} = \hat{T}^a_{N+1} + \hat{T}^b_{N+1} + \hat{T}^c_{N+1}$ is defined by,

$$\hat{T}^a_{N+1} = \epsilon_{N+1} \sum_\sigma f^\dagger_{N+1\sigma} f_{N+1\sigma} \qquad ; \qquad \hat{T}^b_{N+1} = t_N \sum_\sigma f^\dagger_{N\sigma} f_{N+1\sigma} \qquad ; \qquad \hat{T}^c_{N+1} = t_N \sum_\sigma f^\dagger_{N+1\sigma} f_{N\sigma} \tag{S.10}$$

At step $N+1$ of the iterative diagonalization process, we add on the new Wilson chain site $|k\rangle_{N+1}$, where the index $k = \{0, -1, +1, 2\}$ labels the four possible configurations of that site, $|k\rangle_{N+1} = \{|-\rangle, |\downarrow\rangle, |\uparrow\rangle, |\uparrow\downarrow\rangle\}$ respectively. Since the part of the Hamiltonian describing the Wilson chain is Hermitian, the left and right eigenstates for the isolated Wilson orbital $|k\rangle_{N+1}$ are equal and so we do not specify a L, R superscript. At this step we need to construct the Hamiltonian matrix $\mathbf{H}^b_{N+1}$ with the following matrix elements,

$$[\mathbf{H}^b_{N+1}]_{kr,k'r'} = \langle N+1; k; r|^L_b \, \hat{H}_{N+1} \, |N+1; k'; r'\rangle^R_b \tag{S.11}$$

where the b subscript denotes that these are *basis* states (rather than eigenstates), which are decomposed as,

$$|N+1; k; r\rangle^{L(R)}_b = |k\rangle_{N+1} \otimes |N; r\rangle^{L(R)}_d \tag{S.12}$$

for left(right) basis states. The latter are given in terms of the left(right) eigenstates in the *diagonal* representation (d subscript) of the previous iteration, denoted $|N; r\rangle^{L(R)}_d$. Therefore, these satisfy $\hat{H}_N |N; r\rangle^R_d = E_N(r) |N; r\rangle^R_d$ and $\langle N; r|^L_d \hat{H}_N = \langle N; r|^L_d E_N(r)$ where $E_N(r)$ are the complex eigenvalues of the previous iteration.

We therefore have four terms to compute from Eqs. (S.9), (S.10):

$$\langle k|_{N+1} \langle N;r|_d^L \hat{H}_N |k'\rangle_{N+1} |N;r'\rangle_d^R \ , \tag{S.13}$$
$$\langle k|_{N+1} \langle N;r|_d^L \hat{T}^a_{N+1} |k'\rangle_{N+1} |N;r'\rangle_d^R \ , \tag{S.14}$$
$$\langle k|_{N+1} \langle N;r|_d^L \hat{T}^b_{N+1} |k'\rangle_{N+1} |N;r'\rangle_d^R \ , \tag{S.15}$$
$$\langle k|_{N+1} \langle N;r|_d^L \hat{T}^c_{N+1} |k'\rangle_{N+1} |N;r'\rangle_d^R \ . \tag{S.16}$$

Since $\hat{H}_N$ comprises only even products of operators and does not act on degrees of freedom in orbital $N+1$, Eq. (S.13) simplifies to:

$$\langle k|k'\rangle_{N+1} \langle N;r|_d^L \hat{H}_N |N,r'\rangle_d^R = \delta_{kk'} \langle N;r\ |N;r'\rangle_d^{L,R} E_N(r') = \delta_{kk'}\delta_{rr'}E_N(r) \ . \tag{S.17}$$

Similarly, in Eq. (S.14) $\hat{T}^a_{N+1}$ consists of a number operator acting only on degrees of freedom of orbital $N+1$ and so reduces to,

$$\langle k|_{N+1} \hat{T}^a_{N+1} |k'\rangle_{N+1} \langle N;r|N;r'\rangle_d^{L,R} = \delta_{kk'}\delta_{rr'}\epsilon_{N+1}|k| \ , \tag{S.18}$$

where we used the fact that when using our convention for the index k, the spin-summed occupation number for state $|k\rangle_{N+1}$ in orbital $N+1$ is $n_k = |k|$.

Eqs. (S.15) and (S.16) are more complicated since they connect the part of the chain spanned by $\hat{H}_N$ to the added orbital $N+1$. To make progress we insert the identity,

$$\mathbb{1}_{N+1} = \sum_{m,s} |m\rangle_{N+1} |N;s\rangle_d^R \langle N;s|_d^L \langle m|_{N+1} \ , \tag{S.19}$$

between the creation and annihilation operators of $\hat{T}^b_{N+1}$ and $\hat{T}^c_{N+1}$ in Eq. (S.10). Then Eq. (S.15) becomes,

$$\begin{aligned} & t_N \sum_{\sigma,m,s} \langle N;r|_d^L \langle k|_{N+1} f^\dagger_{N\sigma} |m\rangle_{N+1} |N;s\rangle_d^R \langle N;s|_d^L \langle m|_{N+1} f_{N+1\sigma} |k'\rangle_{N+1} |N;r'\rangle_d^R && \text{(S.20)}\\ =& t_N \sum_{\sigma,m,s} (-1)^k \langle k|m\rangle_{N+1} \langle N;r|_d^L f^\dagger_{N\sigma} |N;s\rangle_d^R \cdot \langle m|_{N+1} f_{N+1\sigma} |k'\rangle_{N+1} \cdot \langle N;s|N;r'\rangle_d^{L,R} && \text{(S.21)}\\ =& t_N \sum_{\sigma} (-1)^k M^\sigma_{k,k'} \cdot \langle N;r|_d^L f^\dagger_{N\sigma} |N;r'\rangle_d^R \ , && \text{(S.22)} \end{aligned}$$

where we have defined $M^\sigma_{k,k'}$ to denote the matrix element $\langle k|_{N+1} f_{N+1\sigma}|k'\rangle_{N+1}$, which is independent of the value of N. Note also that $(M^\sigma_{k,k'})^\dagger = M^\sigma_{k',k}$. The factor of $(-1)^k$ comes from the fermionic anticommutation when reordering operators.

Similarly for Eq. (S.16), we obtain,

$$t_N \sum_{\sigma} (-1)^{k'} M^\sigma_{k',k} \cdot \langle N;r|_d^L f_{N\sigma} |N;r'\rangle_d^R \ . \tag{S.23}$$

The nontrivial matrix elements $\langle N;r|_d^L f^\dagger_{N\sigma} |N;r'\rangle_d^R$ and $\langle N;r|_d^L f_{N\sigma} |N;r'\rangle_d^R$ must be computed at the previous step and saved. Note that they are not simple Hermitian conjugates of each other and must be calculated separately.

From these expressions, one may construct the NH Hamiltonian $\hat{H}_{N+1}$ at step $N+1$ from information obtained at step N – specifically, the eigenvalues $E_N(r)$, and the matrix elements $\langle N;r|_d^L f^\dagger_{N\sigma} |N;r'\rangle_d^R$ and $\langle N;r|_d^L f_{N\sigma} |N;r'\rangle_d^R$. With $\mathbf{H}^b_{N+1}$ now constructed, we can diagonalize this matrix to obtain the eigenvalues E_{N+1} and the left and right eigenvectors $|N+1;r\rangle_d^{L(R)}$. In particular, we can write $\mathbf{H}^b_{N+1} = \mathbf{U}^R_{N+1}\mathbf{H}^d_{N+1}(\mathbf{U}^L_{N+1})^\dagger$ where $\mathbf{H}^d_{N+1}$ is the *diagonal* matrix of eigenvalues E_{N+1} and $\mathbf{U}^{R(L)}_{N+1}$ is a matrix whose columns are the right(left) eigenvectors. This provides the set of complex eigenvalues E_{N+1} needed for the next step.

What about the matrix elements of the $f_{N+1\sigma}$ and $f^\dagger_{N+1\sigma}$ operators? These are also needed for the next step. To compute these, we expand the eigenstates as,

$$\begin{aligned} |N+1;r\rangle_d^{R(L)} &= \sum_{m,s} U^{R(L)}_{N+1}(r;m,s)^{(\dagger)} |N+1;m;s\rangle_b^{R(L)} \\ &\equiv \sum_{m,s} U^{R(L)}_{N+1}(r;m,s)^{(\dagger)} |m\rangle_{N+1} |N;s\rangle_d^{R(L)} \ . && \text{(S.24)} \end{aligned}$$

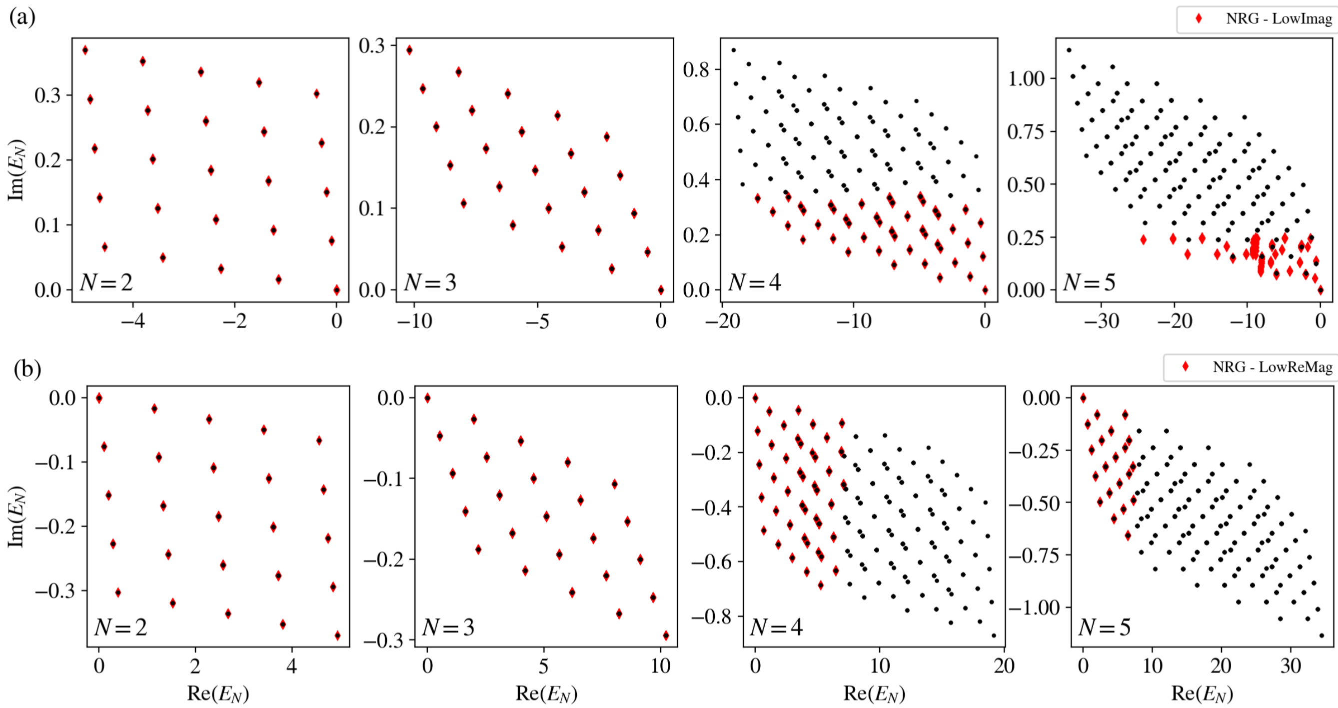

FIG. S1. Illustration of alternate truncation schemes for NH-NRG on the non-interacting ($U_d = 0$) NH AIM (also known as the non-Hermitian RLM). The plots are analogous to those in Fig. E1 of the main text, and the same parameters are used ($\Lambda = 3$, $N_k = 1024$, $\epsilon_d = 0$, $V = 0.1 - 0.08i$). Top row panels (a) show truncation to the lowest N_k states ordered by $\mathrm{Im}(E_N)$; bottom row panels (b) show a hybrid scheme in which the 'ground state' with lowest $\mathrm{Re}(E_N)$ is first subtracted, and then states are sorted by magnitude, $|E_N - E_N^{gs}|$. NH-NRG results as red-diamonds, exact diagonalization results as black circle points.

We use this to construct the matrix element,

$$\langle N+1; r|_d^L \, f^\dagger_{N+1\sigma} \, |N+1; r'\rangle_d^R = \sum_{\substack{m,s \\ m',s'}} U^L_{N+1}(r;m,s)^\dagger U^R_{N+1}(r';m',s') \, \langle N;s|N;s'\rangle_d^{L,R} \, \langle m|_{N+1} \, f^\dagger_{N+1\sigma} \, |m'\rangle_{N+1} \tag{S.25}$$

$$= \sum_{m,m',s} M^\sigma_{m'm} \, U^L_{N+1}(r;m,s)^\dagger U^R_{N+1}(r';m',s) \tag{S.26}$$

and similarly

$$\langle N+1; r|_d^L \, f_{N+1\sigma} \, |N+1; r'\rangle_d^R = \sum_{m,m',s} M^\sigma_{mm'} \, U^L_{N+1}(r;m,s)^\dagger U^R_{N+1}(r';m',s) \tag{S.27}$$

Thus, we have all of the ingredients to proceed to the next step. In this way, the entire chain can be built up orbital by orbital, starting from $\hat{H}_0$, which one explicitly constructs 'by hand' in the initialization step.

Without truncation, the Fock space would of course grow by a factor of four at each iteration. However, due to the exponentially-decaying Wilson chain parameters, we have a scale separation from iteration to iteration that motivates a truncation to just the N_k lowest-lying states at each iteration, meaning that the computational complexity of the NH-NRG calculation scales *linearly* with N rather than exponentially. Of course, with complex eigenvalues E_N at each step, there is a subtlety about what is meant by 'lowest lying', and there are several truncation schemes that one could envision. The simplest, and the one that is closest to that employed in regular Hermitian NRG, is to truncate to the lowest N_k eigenstates ordered by $\mathrm{Re}(E_N)$. This turns out to be the most numerically stable and accurate scheme, which we have confirmed reproduces correctly the exact results of exact diagonalization in the non-interacting limit. These issues are explored in more detail in the following sections.

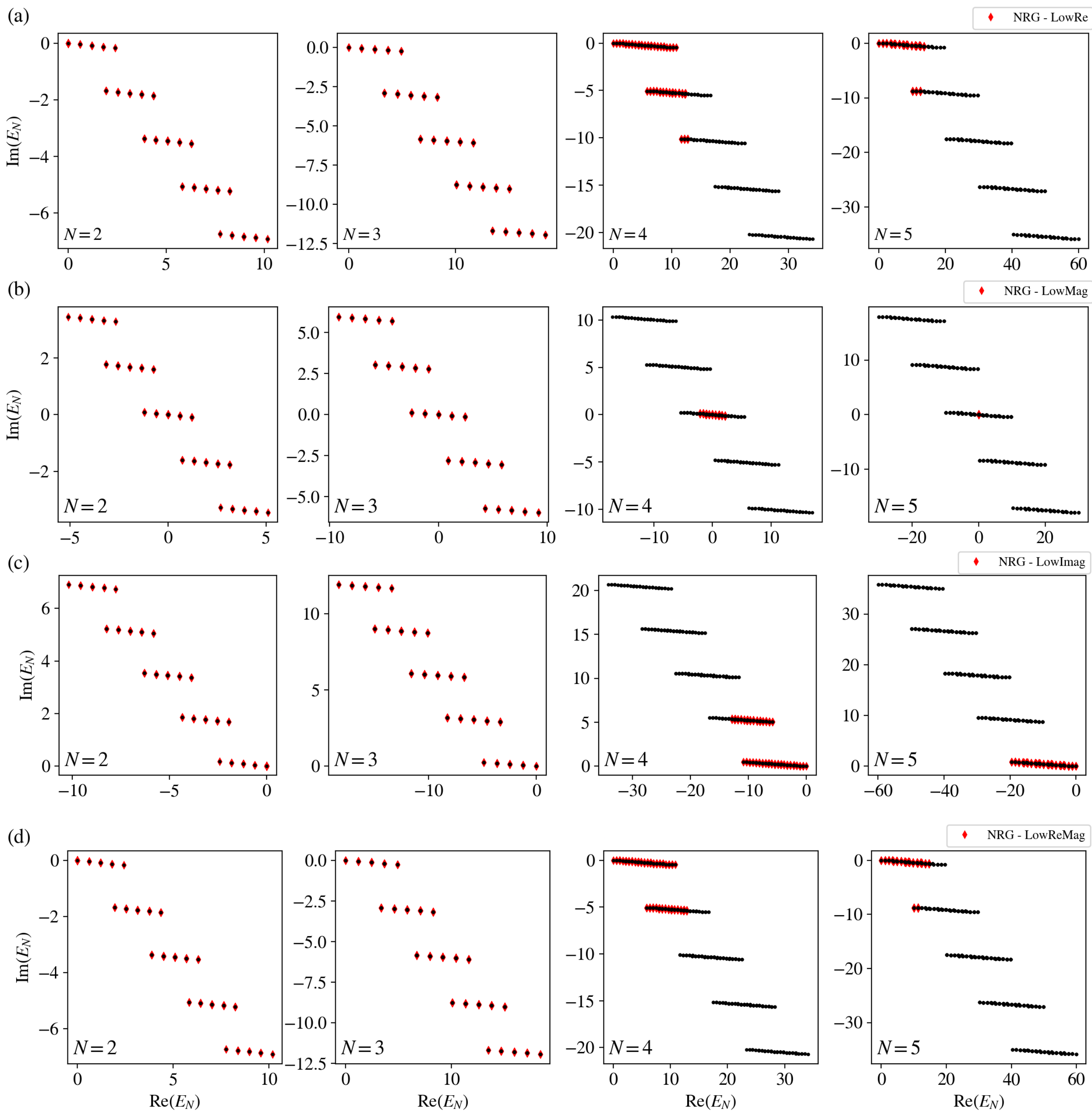

FIG. S2. Analogous plots as shown in Figs. E1 and S1, but here in the strongly non-perturbative regime, far from the Hermitian limit, using $V = 1 - 1i$. All other parameters are kept the same for the purposes of comparison.

S.III. ALTERNATIVE TRUNCATION SCHEMES

S.III.A. Non-Hermitian resonant level model

In the main text, we presented results for strongly-correlated quantum impurity problems obtained by NH-NRG using a truncation scheme ('LowRe') in which the lowest N_k states were kept at each step, sorted by Re(E_N). In the *End Matter* we presented some justification for that, by consideration of the non-interacting limit of the AIM ($U_d = 0$), also known as the 'resonant level model' (RLM). Being quadratic, the RLM can be solved exactly by diagonalizing

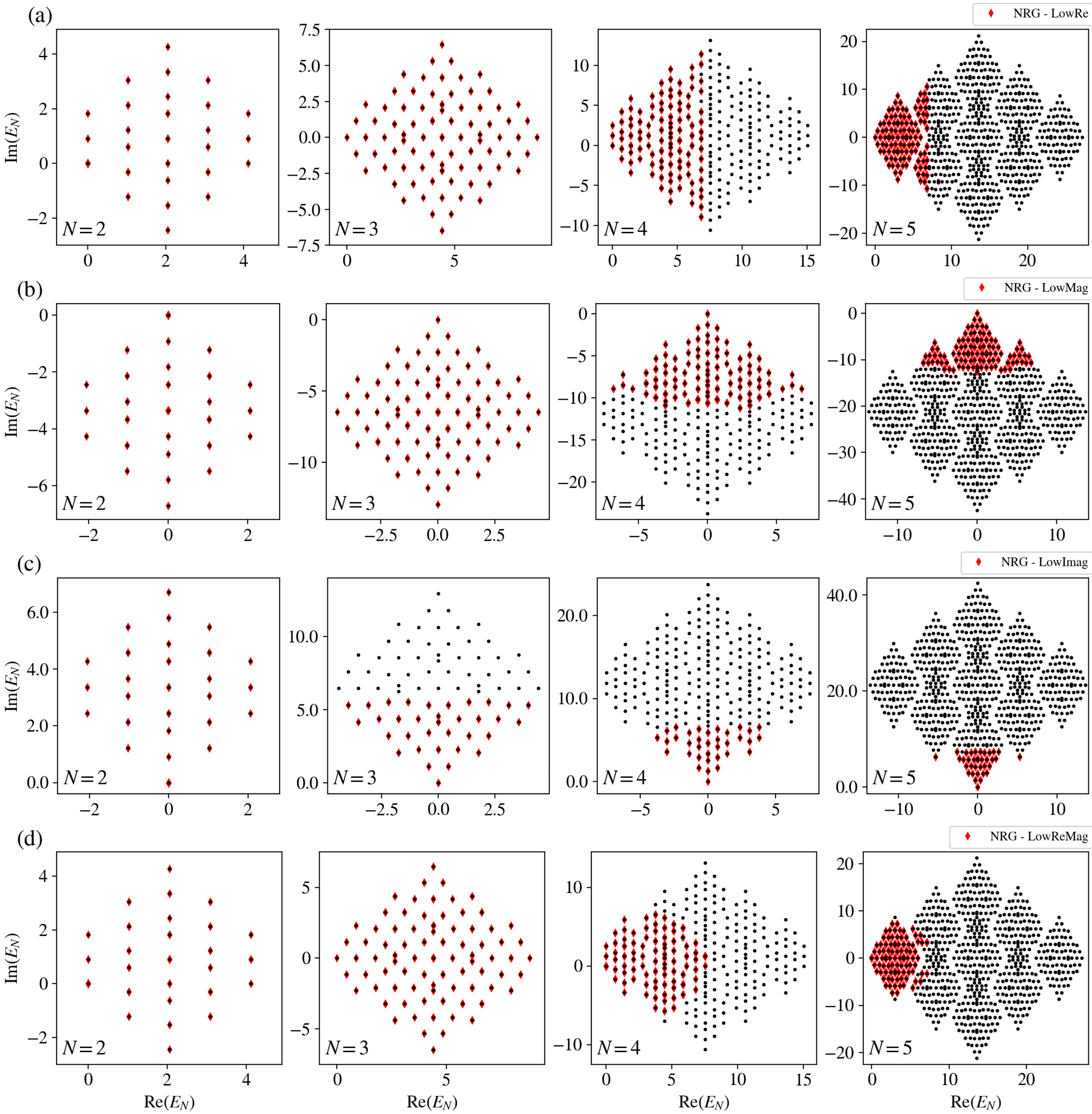

FIG. S3. Illustration of different truncation schemes for NH-NRG for the free Wilson chain with imaginary on-site potentials $\epsilon_n = -it_n$, where t_n are the usual Wilson chain coefficients for a flat conduction band of width $D = 1$. The four truncation schemes discussed in the text are shown, comparing NH-NRG results (red diamonds) with exact diagonalization (black circle points) for the complex eigenvalues of $\hat{H}_N$ for different iterations N. The full spectrum from exact diagonalization is shown in each case; NH-NRG reconstructs a different part of this spectrum due to the different truncation schemes employed. Plotted for $\Lambda = 3$ and $N_k = 400$.

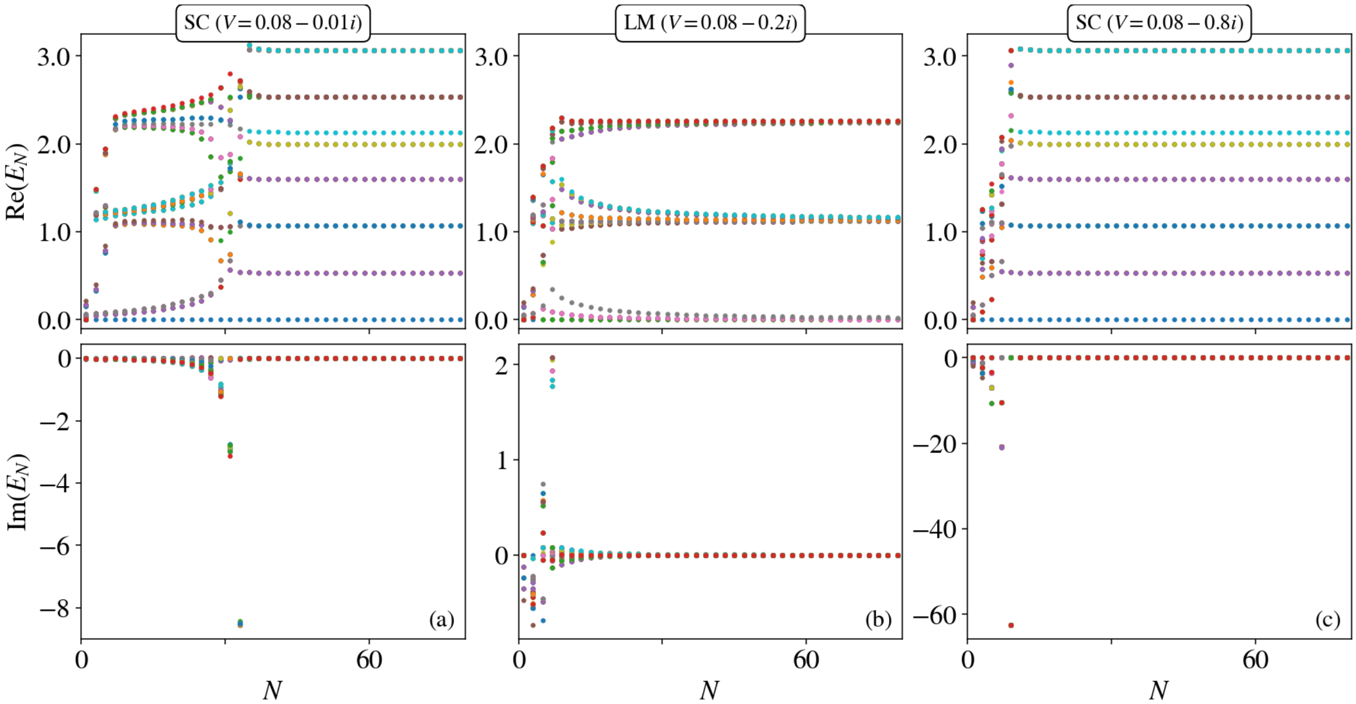

FIG. S4. Non-Hermitian Anderson impurity model ($U_d = 0.3$, $\epsilon_d = -0.15$, $\Lambda = 3$, $N_k = 400$, 128-bit precision): Eigenvalue RG flow diagrams as Im(V) is made more negative, showing (a) SC phase; (b) LM phase; and (c) re-entrant SC phase.

the Hamiltonian in the single-particle sector (an $(N+2) \times (N+2)$ matrix at step N), and then constructing the 4^{N+2} many-particle states as simple product states from these – a trivial combinatorial exercise. As such, the full eigenspectrum of the NH-NRG Hamiltonian $\hat{H}_N$ can be obtained by exact diagonalization for essentially any N of interest, without any truncation, in this non-interacting limit. On the other hand, NH-NRG works in precisely the same way independently of U_d and so the interacting AIM and non-interacting RLM are treated identically from an algorithmic point of view. The non-interacting RLM therefore provides a stringent check of our NH-NRG results. Fig. E1(a) confirmed that truncation by lowest Re(E_N) correctly reproduces the exact eigenvalues at each step, for the retained states. One can also truncate by keeping the N_k states with lowest absolute magnitude of $|E_N|$, as shown in Fig. E1(b) – although in practice we found this to be less numerically stable. We dub this scheme 'LowMag'.

In Fig. S1 we consider two other truncation schemes. In the top row panels (a) we show truncation ('LowImag') to the lowest N_k states ordered by Im(E_N), which targets a different set of kept states. While this method works initially, after a few steps it starts to break down. For $N = 5$ we see that the NH-NRG eigenvalues no longer match those from exact diagonalization. In the bottom row panels Fig. S1(b), we use a hybrid scheme ('LowReMag') in which the 'ground state' with the lowest Re(E_N) is first subtracted, and then states are ordered by their magnitude, $|E_N - E_N^{gs}|$. This truncation scheme also works very well and seems to be both accurate in reproducing the results of exact diagonalization, as well as being numerically stable. In both cases we plot the *rescaled* many-particle eigenvalues, comparing NH-NRG (red diamonds) with exact diagonalization (black circle points).

In Fig. S2 we present the analogous results shown in Figs. E1 and S1, but this time for $V = 1 - 1i$. This is in a strongly non-perturbative regime, far from the Hermitian limit. Again we see precise agreement between exact diagonalization results and NH-NRG, establishing the applicability of NH-NRG in this nontrivial regime. Although here all truncation schemes seem to work well, we found that truncation by the lowest real-part of E_N is still the best choice in terms of numerical stability.

S.III.B. Free Wilson chain with imaginary potentials

As a further demonstration, we consider NH-NRG for the free Wilson chain (no impurity). We introduce non-Hermiticity to the Wilson chain by using complex Wilson chain potentials. Specifically, we choose $\epsilon_n = -it_n$, where t_n are the usual Wilson chain hopping parameters for a metallic flat band with bandwidth $D = 1$ as before. For the Hermitian symmetric flat-band Wilson chain, $\epsilon_n = 0$, so introducing imaginary potentials down the chain simulates

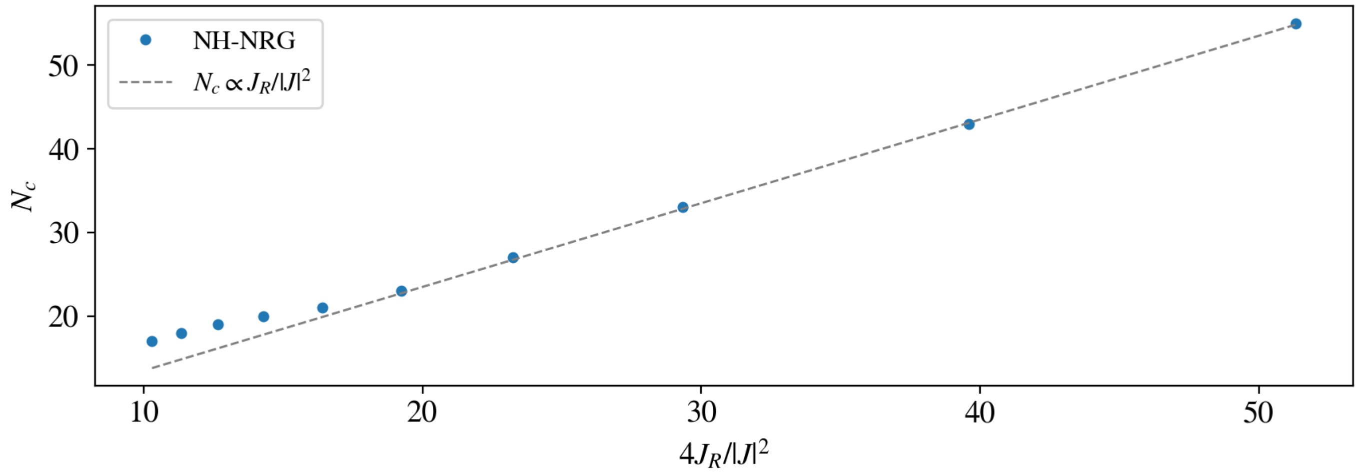

FIG. S5. Kondo temperature for the non-Hermitian Kondo model at weak coupling. The crossover iteration N_c between LM and SC fixed points is extracted from NH-NRG eigenvalue flow diagrams for various J_R and J_I in the weak coupling (small $|J|$) regime. Shown for $\Lambda = 3$, $N_k = 400$.

a kind of *open* Wilson chain where each site is subject to dissipation and the states have a finite lifetime. Our choice of $\epsilon_n = -it_n$ corresponds to a strong non-Hermitian perturbation on the scale of the bandwidth, and is therefore a stringent check. This setup can be treated in NH-NRG very simply – in practice we project out the impurity by setting $U_d = V = 0$ and $\epsilon_d \gg D$. The resulting NH Wilson chain is simply a non-interacting tight-binding chain and can be solved exactly as per the results in the previous section. In Fig. S3 we compare NH-NRG results (red diamonds) with those of exact diagonalization of the tight-binding model (black circle points), for the four truncation schemes discussed above. We again give results for the *rescaled* many-particle eigenvalues. The results vividly show that NH-NRG works well in all cases, just reconstructing different parts of the spectrum when different truncation schemes are used.

S.IV. ADDITIONAL ANDERSON IMPURITY MODEL DATA

In the main text we presented NH-NRG results for the NH AIM. Here in Fig. S4 we show that by increasing the magnitude of the imaginary part of the impurity-bath hybridization V, one first observes a quantum phase transition from SC to LM, and then back to SC. This re-entrant Kondo behavior is predicted from the NH Kondo model (see Fig. 1(a) of the main text), but is also accessible in the parent AIM. For strong enough $\mathrm{Re}(V)$ the LM phase disappears entirely. Thus the topology of the phase diagrams for Kondo and Anderson models is the same (albeit that naturally the details are somewhat different). This lends further support to the mapping between AIM and Kondo in the non-perturbative strong-coupling regime beyond Schrieffer-Wolff.

We note that the Schrieffer-Wolff transformation between dissipative AIM and NH Kondo model derived in Ref. [6] gives strictly antiferromagnetic $\mathrm{Re}(J) > 0$ and $\mathrm{Im}(J) < 0$. This is the regime we focused on for the NH Kondo model in Fig. 1. With NH-NRG we indeed found that the ferromagnetic regime $\mathrm{Re}(J) < 0$ was not accessible within the NH AIM. However, the ferromagnetic NH Kondo model might be interesting to study in its own right. We leave this to future work.

S.V. KONDO TEMPERATURE

Here, we numerically extract the crossover iteration number N_c, characterizing the flow between LM and SC fixed points from the RG flow diagrams of the NH-NRG. In Fig. S5, we plot the extracted N_c as a function of the complex coupling $J = J_R - iJ_I$. At weak coupling (large N_c), we find excellent agreement with the predicted form of T_K discussed in the main text. The running NRG energy scale [7] is given by $E \sim D\Lambda^{-N/2}$ and so we identify the Kondo 'temperature' $T_K \sim D\Lambda^{-N_c/2}$ in terms of the crossover iteration N_c. Our data is consistent with the relation $T_K \sim De^{-2DJ_R/|J|^2}$ which implies $N_c = a + bJ_R/|J|^2$ with a an irrelevant constant that depends on the specific definition of T_K used, and $b = 4/\ln\Lambda$. The behavior of T_K at stronger coupling was found to be more complicated.

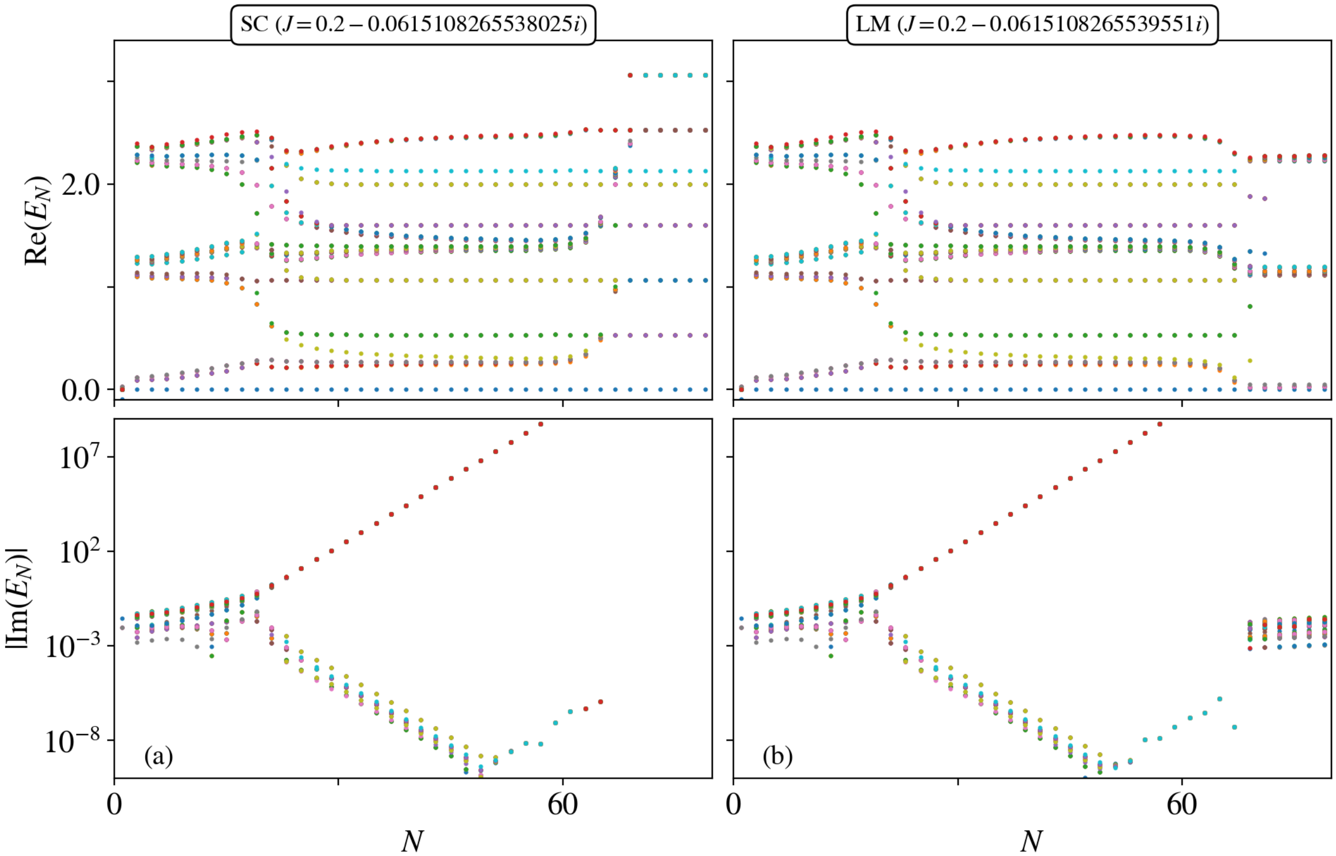

FIG. S6. RG flow of the NH-NRG complex eigenvalues E_N with iteration number N, showing the real and imaginary parts in the top and bottom panels, for representative systems in the SC (a) and LM (b) phases. Shown for $\Lambda = 3$, $N_k = 200$ at 128-bit precision.

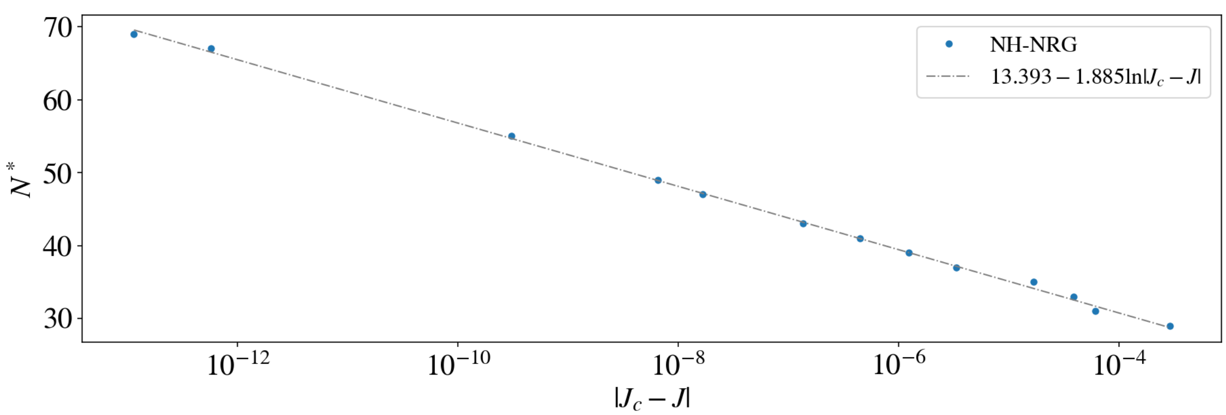

FIG. S7. Crossover scale for the non-Hermitian Kondo model near critical coupling. The crossover iteration N^* between LM and SC fixed points is extracted from NH-NRG eigenvalue flow diagrams for various J_R and J_I in the regime of critical coupling J_c. Shown for $\Lambda = 3$, $N_k = 200$ at 128-bit precision.

S.VI. CRITICAL POINT OF THE NH KONDO MODEL

In the main text we identified a phase transition in the metallic NH Kondo model between SC and LM phases for $J_R > 0$ as a function of J_I. In Fig. S6 we show the RG flow on either side of the transition at $J = J_c$, obtained by NH-NRG. We tune J_I very close to the transition in both cases, and see an extended RG flow in the vicinity of a

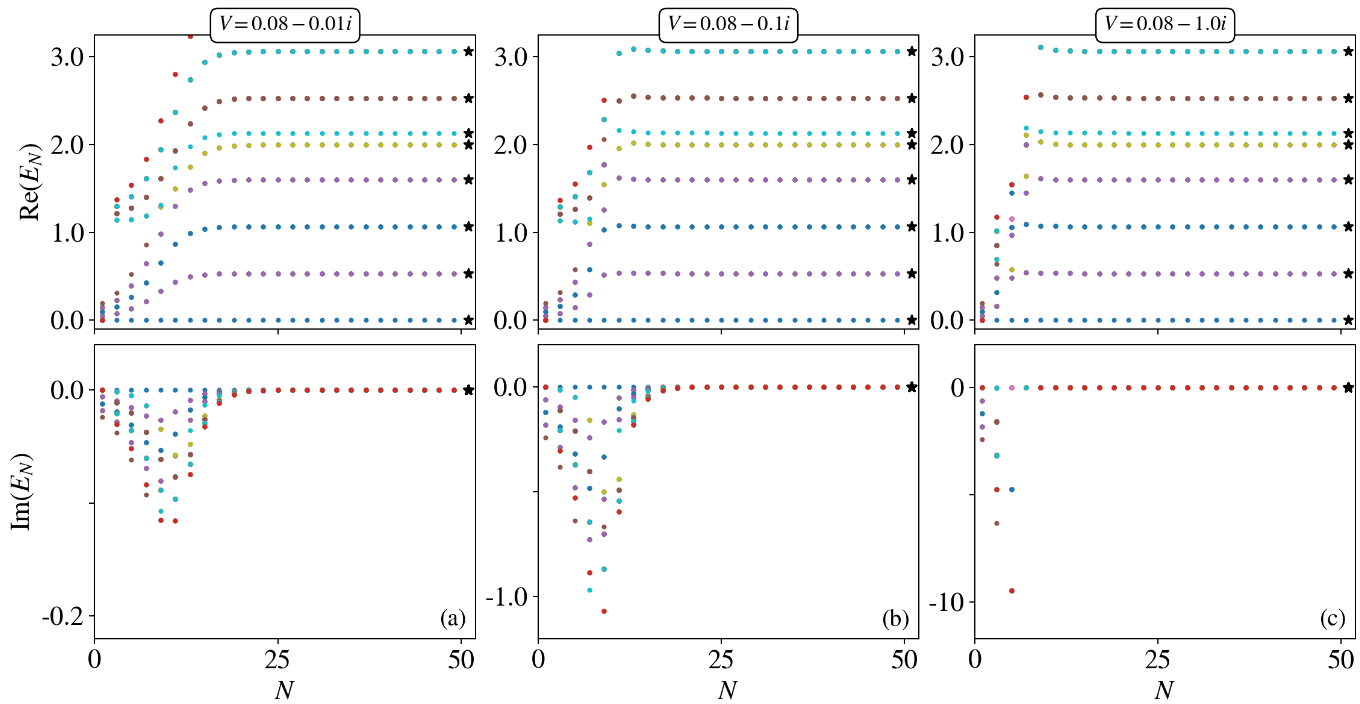

FIG. S8. Eigenvalue RG flows in the non-interacting limit of the NH AIM ($U_d = \epsilon_d = 0$), obtained by NH-NRG. Star points show comparison to exact diagonalization results. For any value of ImV we see the same low-energy SC physics. Finite U_d is required to stabilize the LM phase. Computed using $\Lambda = 3$ and $N_k = 600$.

novel critical fixed point. The critical fixed point is not of LM or SC type, and cannot be understood as a simple mixture of LM and SC states. In particular, we see a diverging imaginary part to the NRG energy levels at the critical point, with Im(E_N) growing exponentially with N. When the system eventually crosses over to either SC or LM, the imaginary part of the eigenvalues disappears, and the usual Hermitian Kondo fixed point structures emerge. We therefore conclude that the transition is controlled by an unusual non-Hermitian critical fixed point.

In the vicinity of the transition near J_c, we identify a critical scale T^* that vanishes as the transition is approached. From the NH-NRG data we identify a crossover iteration number N^* for flow from the critical fixed point to either the LM or SC fixed points. In Fig. S7 we show the evolution of N^* with $|J - J_c|$, confirming the scaling behavior $N^* = a - b \ln |J - J_c|$. Since the corresponding crossover energy scale in NRG is $T^* \sim \Lambda^{-N^*/2}$, we may write $T^* \sim |J - J_c|^s$ with $s = \frac{1}{2} b \ln(\Lambda)$. With $\Lambda = 3$ we extracted $b = 1.885$ which yields $s \simeq 1$. Although for Hermitian systems this scaling might suggest a first-order transition, the appearance of a distinct critical fixed point here indicates otherwise. The non-Hermitian critical point appears to be rather exotic, possibly connected with an exceptional point of the model. A full understanding clearly requires further detailed study, which we leave for future work.

S.VII. PHYSICAL INTERPRETATION OF RE-ENTRANT STRONG-COUPLING BEHAVIOR AND CONTINUITY TO THE NON-INTERACTING LIMIT

The Hermitian Kondo model (Eq. 1 with $J_I = 0$) is characterized by an RG flow to the strong-coupling (SC) fixed point for any $J_R > 0$ [7]. This is associated with the formation of a Kondo spin-singlet state between the impurity spin-$\frac{1}{2}$ and the (renormalized) Wilson orbital $f_{0\sigma}$. At low energies $\ll T_K$ the physics can be described in terms of a (nearly) free Wilson chain, with the impurity and the $f_{0\sigma}$ orbital effectively removed, or frozen out. This is the Fermi-liquid picture, in which the low-energy physics can be viewed in terms of a free conduction electron system with a modified boundary condition, corresponding to a $\pi/2$ scattering phase shift [4].

Since the exchange coupling J lives on the bond between the impurity spin and the Wilson zero-orbital $f_{0\sigma}$, dissipative effects modeled by finite $J_I > 0$ in the non-Hermitian case can localize the $f_{0\sigma}$ orbital as well as the impurity, if sufficiently strong. For small $J_I \ll J_R$, the Kondo effect dominates and the impurity spin is screened by conduction electrons, leading to a ground state described by the SC fixed point as per the Hermitian case. At larger

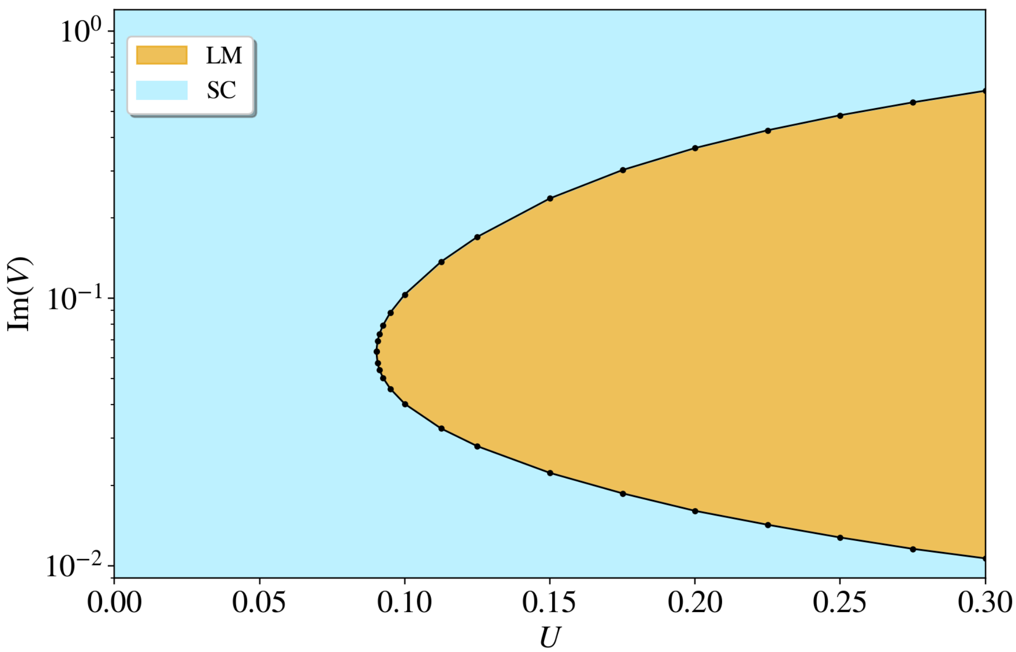

FIG. S9. Phase diagram for the NH AIM for finite Re$V = 0.08$ as a function of U_d and ImV, computed using NH-NRG ($\Lambda = 3$ and $N_k = 600$). A single SC phase continuously connects states at large and small ImV with the non-interacting limit $U_d \to 0$.

J_I, dissipation tends to localize the impurity spin, freezing it out [8]. However, if $J_I \ll D$ then strong electronic tunneling into the site $f_{0\sigma}$ from the rest of the bath will keep this site *delocalized*. This state is described by the local moment (LM) fixed point – a free Wilson chain with only the impurity removed (zero phase shift). But when $J_I \gg D$, both the impurity and the bath site $f_{0\sigma}$ are localized. At low energies, this again corresponds to a free Wilson chain with one site removed. Therefore at large J_I we expect to recover the SC fixed point behavior – even though the mechanism is quite different for small and large J_I. We see in Fig. 1a of the main text that in fact these two regimes are continuously connected (without an intervening phase transition) by going to large J_R past J_R^* where the LM phase terminates. The re-entrant SC behavior at large J_I is in fact just one region of a single SC phase, shared with Kondo SC physics at $J_I = 0$. The SC fixed point structure is identical throughout this phase.

This behavior is more plainly understood in the AIM, which features a correlated fermionic impurity site (rather than a strict spin-$\frac{1}{2}$), tunnel-coupled by V to the bath. In the non-Hermitian variant, the V is complex, see Eq. 2 of the main text. The NH Kondo model is the low-energy effective model for the NH AIM when the impurity is singly-occupied (see Fig. 3 of the main text) and they share the same underlying physics and fixed points in this regime. The $U_d = 0$ non-interacting limit of the AIM can be solved exactly without approximation by exact diagonalization in the single-particle sector, followed by simple reconstruction of the many-particle (product) states. In this limit, we find SC physics for *all* values of the complex coupling V. This is illustrated in Fig. S8, where NRG results are compared with exact diagonalization results (star points), for different ImV. We conclude that a finite correlation strength U_d is required to stabilize the LM phase. At $U_d = 0$ we have no LM physics and we have an SC ground state independently of the strength of the dissipation described by ImV. This shows that indeed the Kondo-screened state (e.g. at Im$V = 0$ and Re$V > 0$) and the dissipation-induced localized state (e.g. at Re$V = 0$ and Im$V > 0$) are equivalent and continuously connected through a single SC phase.

However, we see no re-entrant SC behavior in the non-interacting limit $U_d = 0$ because there is no intervening LM phase. Our argument is completed by considering continuity of the interacting AIM to the non-interacting limit as $U_d \to 0$. In Fig. S9 we take fixed Re$V = 0.08$ and map out the phase diagram as a function of U_d. Here we immediately see that the re-entrant SC behavior at large ImV is not only connected to the Kondo SC behavior at small (and even zero) ImV, but it is also shared by the non-interacting limit $U_d = 0$ for which we have an exact solution. Interestingly, for any finite ReV, we have a finite, minimum critical U_d^* below which the LM phase vanishes.

To further emphasize this point, in Fig. S10 we show how the re-entrant SC behavior at finite U_d and large ImV is identical to that obtained at $U_d = 0$, in terms of RG eigenvalue flows. The re-entrant SC behavior is therefore understandable as part of a single SC phase in the higher-dimensional space of V and U_d, and is present already in the exactly-solvable non-interacting limit. This description is obscured in the original NH Kondo model because any finite J can be regarded in some sense as being strongly interacting, and the impurity local moment is presupposed.

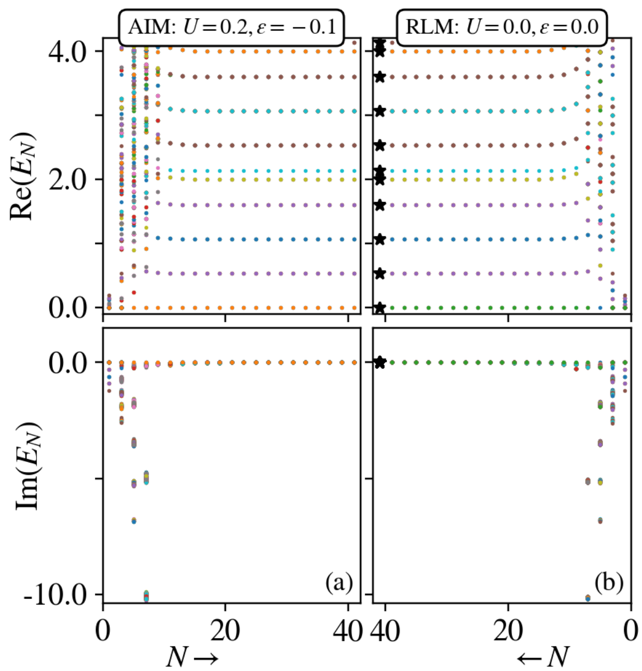

FIG. S10. Comparison of NH-NRG eigenvalue flows in the interacting (a) and non-interacting (b) AIM. The latter is compared with exact diagonalization results for the fixed point (star points). Computed using $\Lambda = 3$, $N_k = 600$, and $V = 0.08 - 0.5i$.

Our conclusion is that finite U_d is required to realize the LM phase in the NH AIM. The LM phase shrinks and vanishes in the non-interacting limit $U_d \to 0$. The SC physics at finite U_d can therefore be understood in terms of Fermi liquid theory as a renormalized version of the exactly-solvable $U_d = 0$ SC state, even in the non-Hermitian case of finite ImV.

S.VIII. CONVERGENCE OF NH-NRG RESULTS AS $\Lambda \to 1$

As explained in the main text, at the heart of the NRG approach is a logarithmic discretization of the free continuum bath density of states, controlled by the discretization parameter Λ [7]. This represents a coarse-graining in which some bath states are thrown away. However, as shown by Wilson in the seminal paper Ref. [7], the neglected states couple only indirectly and weakly to the impurity; the fixed points, emergent scales, and RG flows are rather insensitive to the choice of Λ when $\Lambda > 1$. Although $\Lambda = 1$ corresponds to the exact, non-discretized model, $\Lambda > 1$ is needed to justify the Fock-space truncation at each step – itself required to avoid exponential complexity scaling of the NRG calculation with increasing N. Indeed, while discretization artifacts get worse with increasing Λ, the energy-scale separation and therefore the validity of truncation gets better with increasing Λ. Therefore NRG constitutes a compromise where a finite value $\Lambda > 1$ is chosen. As Wilson remarkably showed, this compromise still leads to essentially exact results for calculated physical quantities due to the RG structure of the problem and universality – provided enough states N_k are kept in the calculation at each step. Values of $\Lambda = 2$–3 are very standard, but much larger values have also been successfully used in the literature [9]. We illustrate this fact in Fig. S11 where we use our NRG implementation to compute the impurity entropy as a function of temperature for the AIM in the Hermitian limit, Im$V = 0$, taking different values of Λ. Computed thermodynamic quantities such as this are essentially invariant to decreasing Λ and are well-converged.

Turning now to NH-NRG and our solution of the NH Kondo model, we used $\Lambda = 3$ to obtain the results presented in the main text. Similarly to the Hermitian limit, the RG flows in the majority of the phase diagram were found to be very insensitive to the choice of Λ. However, close to the SC/LM quantum phase transition, the system becomes sensitive to small perturbations. Especially for large values of $|J|$ near the upper (re-entrant) transition, we found some small drift in the extracted value of the critical J_I^* upon decreasing Λ towards $\Lambda = 1$. We emphasize that the qualitative behavior is unchanged, and that the $\Lambda \to 1$ limit can be taken numerically to extract the "true" critical couplings. Our analysis showing the effect of reducing Λ on the phase diagram is shown in Fig. S12. The critical couplings for the lower transition are essentially already well-converged using $\Lambda = 3$. For the upper transition, J_I^* increases slightly as $\Lambda \to 1$, but remain well-behaved and finite in this limit.

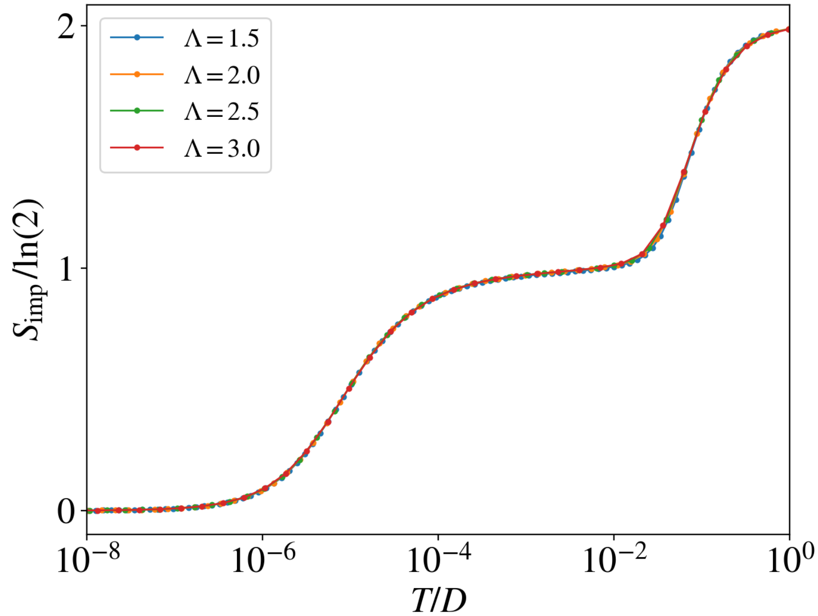

FIG. S11. NRG results for the AIM in the Hermitian limit, showing the impurity contribution to the entropy $S_{\rm imp}(T)$ vs temperature T. Calculations done using discretization parameter $\Lambda = 1.5, 2, 2.5, 3$, showing extremely well converged results that are largely insensitive to the specific value of Λ chosen. Here we use $U_d = 0.3$, $\epsilon_d = -0.15$, $V = 0.1$ and $N_k = 6000$.

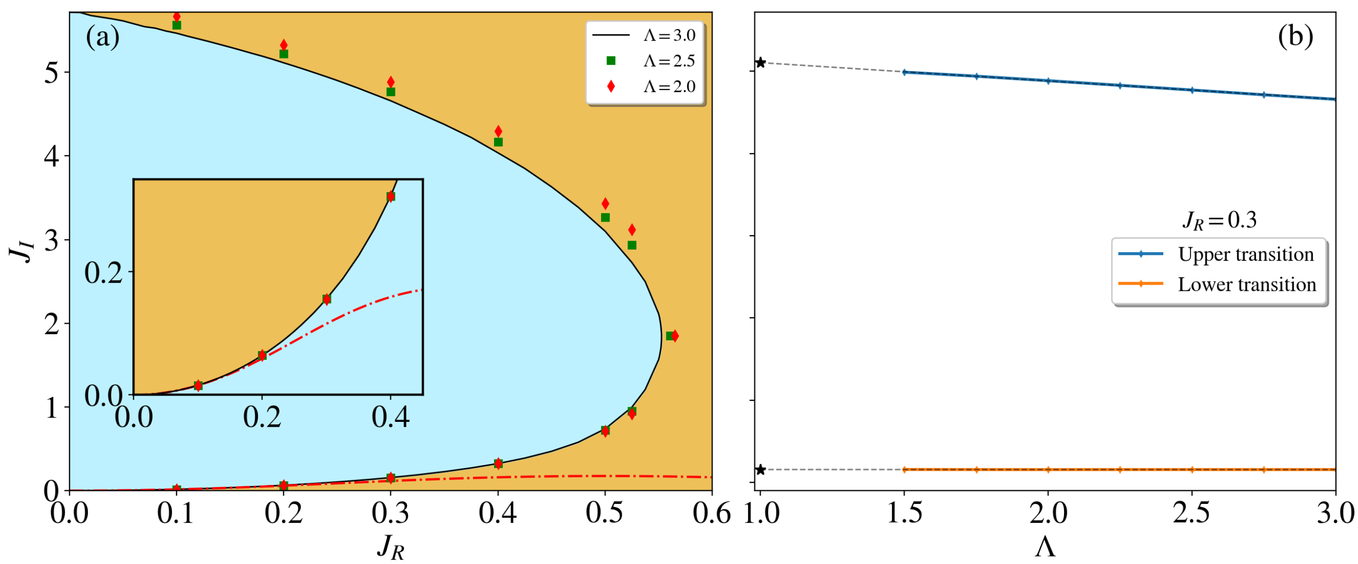

FIG. S12. (a) Companion of Fig. 1a of the main text, in which we show NH-NRG results for the SC/LM phase diagram of the NH Kondo model in the (J_R, J_I) plane. Results obtained using $\Lambda = 3$ (lines) are here compared with those obtained using $\Lambda = 2.5$ and $\Lambda = 2$ (points). The qualitative behavior and topology of the phase diagram is unchanged, but at larger $|J|$ we observe some drift in the extracted critical values J^* separating SC (orange) from LM (blue). (b) Convergence of J_I^* to the $\Lambda \to 1$ limit for $J_R = 0.3$. The critical values extrapolated to $\Lambda = 1$ are indicated with star points, and remain finite.

S.IX. IMPURITY MAGNETIZATION

In the main text, we present eigenvalue RG flow diagrams that illustrate the flow to stable fixed points. To further confirm the presence of the phase transitions between the SC and LM (and LM to SC) phases that we observe, here we present initial findings for the ground-state (zero “temperature”) impurity magnetization, calculated using the Anders-Schiller basis [10] employed in full-density-matrix NRG [11]. This quantity has been studied in recent works

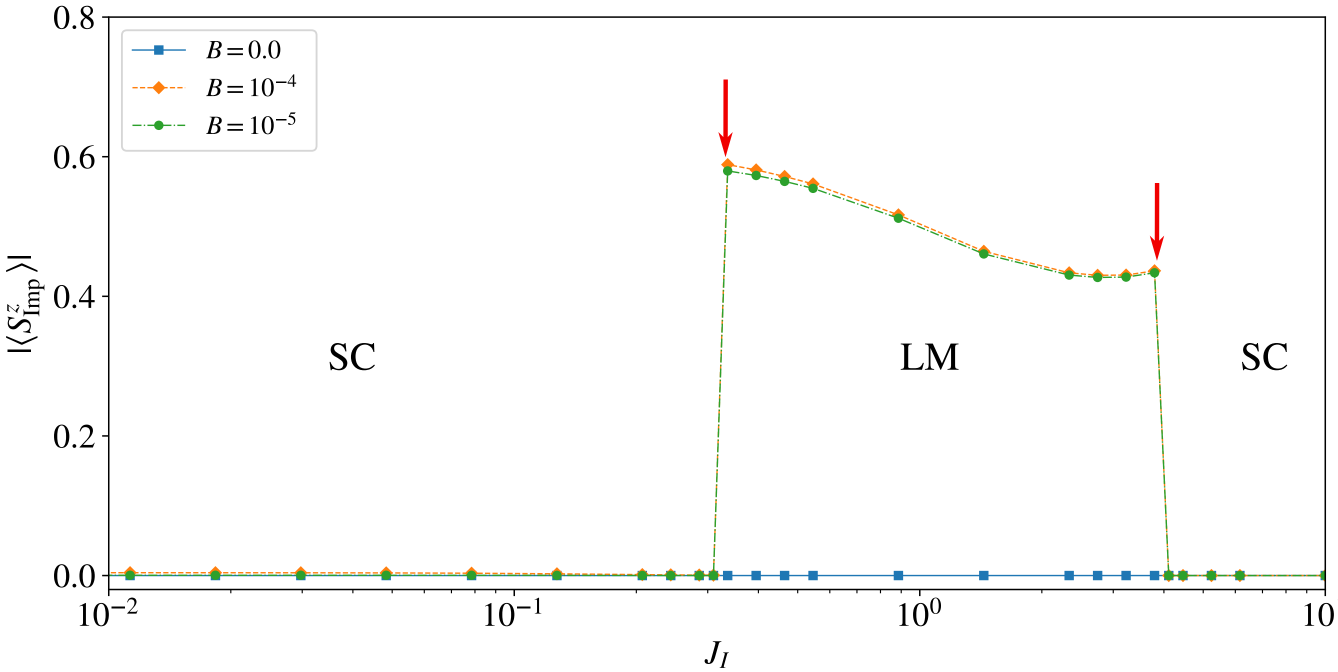

FIG. S13. $|\langle S^z_{\rm Imp}\rangle|$ for the NH Kondo model with the impurity subject to a small Zeeman field B along z, calculated in the ground state using the full-density-matrix NRG method, established on the complete Anders-Schiller basis. NH-NRG calculations performed for $J = 0.4 - iJ_I$, $\Lambda = 3$, $N_k = 600$, and 100 iterations. Arrows indicate the phase boundaries found in Fig. 1a of the main text.

on dissipative impurity systems [8, 12]. In the strong-coupling (SC) fixed-point regime, one expects the impurity magnetization to be near zero, whereas in the local-moment (LM) regime, the impurity spin should polarize in alignment with the on-site magnetic field.

In Fig. S13, we present results for the impurity magnetization in the NH Kondo model. We plot the magnitude of the impurity magnetization as a function of the imaginary component of the impurity-bath coupling, J_I, for fixed $J_R = 0.4$ and for various magnetic field strengths, B. At small but finite magnetic field, the magnetization begins close to zero, indicating the system is initially in the SC regime, since the field cannot overcome the impurity-bath binding energy, essentially set by the Kondo scale T_K. At larger J_I, the system undergoes a transition to the LM regime, with the magnetization jumping abruptly to approximately $\frac{1}{2}$, indicating that the impurity spin is easily polarizable, and essentially free. Upon further increasing J_I, the system exhibits re-entrant Kondo behavior, and the magnetization returns to approximately zero. We note that the magnetization exceeding $\frac{1}{2}$ can likely be understood in analogy with the impurity density per spin being larger than unity, as discussed in [13]. In the absence of any magnetic field, the impurity magnetization remains zero regardless of fixed point regime, by symmetry. Such static physical quantities, as well as dynamics, will be studied in detail in a follow-up paper.

[1] D. C. Brody, Biorthogonal quantum mechanics, Journal of Physics A: Mathematical and Theoretical **47**, 035305 (2013).
[2] E. Edvardsson, J. L. K. König, and M. Stålhammar, Biorthogonal renormalization (2023), arXiv:2212.06004 [quant-ph].
[3] S.-S. B. Lee and A. Weichselbaum, Adaptive broadening to improve spectral resolution in the numerical renormalization group, Phys. Rev. B **94**, 235127 (2016).
[4] A. C. Hewson, *The Kondo Problem to Heavy Fermions* (Cambridge University Press, 1993).
[5] I. Affleck, A. W. W. Ludwig, and B. A. Jones, Conformal-field-theory approach to the two-impurity Kondo problem: Comparison with numerical renormalization-group results, Phys. Rev. B **52**, 9528 (1995).
[6] M. Vanhoecke and M. Schirò, Kondo-Zeno crossover in the dynamics of a monitored quantum dot, Nature Communications **16**, 6155 (2025).
[7] K. G. Wilson, The renormalization group: Critical phenomena and the Kondo problem, Reviews of Modern Physics **47**, 773–840 (1975).
[8] M. Nakagawa, N. Kawakami, and M. Ueda, Non-Hermitian Kondo effect in ultracold alkaline-earth atoms, Phys. Rev. Lett. **121**, 203001 (2018).

[9] R. Bulla, T. A. Costi, and T. Pruschke, Numerical renormalization group method for quantum impurity systems, Rev. Mod. Phys. **80**, 395 (2008).

[10] F. B. Anders and A. Schiller, Real-time dynamics in quantum-impurity systems: A time-dependent numerical renormalization-group approach, Phys. Rev. Lett. **95**, 196801 (2005).

[11] A. Weichselbaum and J. von Delft, Sum-rule conserving spectral functions from the numerical renormalization group, Phys. Rev. Lett. **99**, 076402 (2007).

[12] P. Kattel, P. R. Pasnoori, J. H. Pixley, and N. Andrei, Spin chain with non-Hermitian $\mathcal{PT}$-symmetric boundary couplings: Exact solution, dissipative Kondo effect, and phase transitions on the edge, Phys. Rev. B **111**, 224407 (2025).

[13] T. Yoshimura, K. Bidzhiev, and H. Saleur, Non-Hermitian quantum impurity systems in and out of equilibrium: Noninteracting case, Phys. Rev. B **102**, 125124 (2020).